https://doi.org/10.5194/wes-2026-210
Preprint. Discussion started: 17 November 2026
© Author(s) 2026. CC BY 4.0 License.



eawe european academy of wind energy
Open Access WIND ENERGY SCIENCE DISCUSSIONS

An analytical framework for modelling wind farm wakes under thermal stability and wind veer

Arslan Salim Dar[1] and Erin E. Bachynski-Polić[1]

[1]Department of Marine Technology, Norwegian University of Science and Technology, Professor J. H. L. Vogts veg 1a, 7052 Trondheim, Norway

Correspondence: Arslan Salim Dar (arslan.s.dar@ntnu.no)

Abstract. Conventional analytical wind farm wake models are developed and validated under the assumption of a neutral boundary layer with no wind veer effects. Wake characteristics of wind farms, however, are highly sensitive to thermal stability and wind veer in the atmospheric boundary layer. In this work, we present an analytical modelling framework that can model the wake velocity deficit of a wind farm under different thermal stability, atmospheric turbulence, and wind veer conditions. The modelling framework integrates a physics-based wake expansion model within a veer-aware wake velocity deficit model, and introduces novel relations for cross-stream turbine-modified integral timescales and cross-stream wake-added turbulence intensities. Large-eddy simulations (LES) of a single turbine and a three-turbine array in a range of thermal stability, wind veer, and turbulence conditions are performed to inform and test the modelling framework. In addition, the LES data of semi-infinite wind farms in neutral conditions, as well as at selected times over a diurnal cycle available from the Johns Hopkins University turbulence database, are also used to assess the performance of the proposed framework. Over all the tested scenarios, the analytical framework shows good agreement with the LES data and outperforms a reference analytical framework. The developed analytical framework offers an accurate, yet simple modelling approach for wind farm wake velocity deficit in diverse atmospheric conditions varying in thermal stability, wind veer, occurrence of low-level jets, and turbulence levels.

1 Introduction

As a wind turbine extracts kinetic energy from the wind, it generates a low-speed and high-turbulence region behind it, commonly referred to as the wake. In a wind farm, turbines operating in the wake have less available power and experience higher fatigue loads compared to those operating in the free flow. For instance, the power of a wind farm in fully aligned wake conditions can be reduced by up to 40% (Stevens and Meneveau, 2017; Porté-Agel et al., 2020), whereas fatigue loads on wind turbines operating in the wake can increase by up to 15% (Thomsen and Sørensen, 1999). From a broader perspective, wind farms can also influence local meteorology, as they act as energy sinks and turbulence sources, and can affect the surface fluxes of momentum and scalars (Baidya Roy et al., 2004; Siedersleben et al., 2018). Understanding and predicting the complex nature of interactions between different atmospheric flows and wind farm flows has been identified as one of the grand challenges in the successful expansion of wind energy (Veers et al., 2019).

https://doi.org/10.5194/wes-2026-210
Preprint. Discussion started: 17 November 2026
© Author(s) 2026. CC BY 4.0 License.



eawe european academy of wind energy
Open Access WIND ENERGY SCIENCE DISCUSSIONS

Heating or cooling of the Earth's surface leads to the formation of potential temperature gradients in the flow, which leads to thermal stratification of the boundary layer. Based on thermal stability, the boundary layer is commonly divided into three categories: neutral with negligible potential temperature gradients, convective when the surface is hotter than the air, and stable when the surface is cooler than the air. Thermal stability is one of the key physical mechanisms that affect the mean flow shear, turbulence production, and entrainment processes in the boundary layer. As a consequence, both wind turbine wake characteristics and wind farm power performance depend strongly on thermal stability (see e.g., (Hansen et al., 2012; Dörenkämper et al., 2015; Abkar et al., 2016)). Wind turbine wakes have been shown to recover faster under convective conditions, whereas the rate of recovery slows down under stable conditions compared to neutral conditions (Abkar and Porté-Agel, 2015; Xie and Archer, 2017; Dar et al., 2026). While the effect of thermal stability is often coupled with turbulence intensity, with lower turbulence intensity in a stable flow and higher in a convective flow compared to a neutral one, it has also been shown that for a fixed hub height turbulence intensity, wake recovery is still affected by thermal stability (Du et al., 2021). The magnitude and spatial distribution of turbine-added turbulence kinetic energy are also affected by thermal stability, with the maximum added turbulence kinetic energy occurring closer to the turbine in convective conditions and farther from it under stable conditions compared to the neutral one (Wu et al., 2024). Wake meandering and the size of coherent turbulent structures have also been shown to depend on thermal stability, with convective conditions generally leading to higher meandering and larger coherent structures due to enhanced turbulent mixing, and stable conditions can be associated with lower meandering and smaller coherent structures due to suppressed turbulent mixing (Machefaux et al., 2016; Ning and Wan, 2019; Placidi et al., 2023; Dar et al., 2026).

The rotation of the Earth induces a Coriolis force in the atmosphere, which leads to the formation of an Ekman spiral in the boundary layer (Ekman, 1905). The Coriolis force has been found to significantly impact the power density of large wind farms (Antonini and Caldeira, 2021). It is a latitude-dependent force, with highest magnitude at the poles and zero at the equator. A consequence of the Coriolis force is a change in the wind direction with height called wind veer. The magnitude of wind veer is also a function of thermal stability, with stronger veer under highly stable boundary layers. Wind veer results in a skewed elliptical wake shape and influences the rate of recovery, and turbulence in the wake (Abkar and Porté-Agel, 2016; Churchfield and Sirnivas, 2018). In wind farms, wind veer has been shown to have an impact on the power of downstream turbines (Nouri et al., 2020; Gadde and Stevens, 2019).

The bulk of our present understanding of wind turbine wakes comes from high-fidelity numerical simulations, wind tunnel experiments, and field measurements (Stevens and Meneveau, 2017; Porté-Agel et al., 2020), which require extensive resources and time. For most practical applications, computationally inexpensive and fast estimation of key wake characteristics is needed (Meneveau, 2019), which is offered by analytical wake models. For wake velocity deficit within and downstream of a wind farm, the analytical models commonly take a two-step approach: they first compute the wake of individual turbines while accounting for changing inflow conditions within a wind farm, followed by superposition of these individual wakes to yield a final three-dimensional wind farm wake.

A number of analytical models have been proposed over the years for individual turbine wakes. These models take advantage of conservation laws, wake self-similarity, and a shape function to determine the wake velocity deficit behind a wind

https://doi.org/10.5194/wes-2026-210
Preprint. Discussion started: 17 November 2026
© Author(s) 2026. CC BY 4.0 License.



eawe european academy of wind energy
Open Access WIND ENERGY SCIENCE DISCUSSIONS

turbine. Early wake models were developed and validated under neutral flow conditions (Jensen, 1983; Frandsen et al., 2006; Bastankhah and Porté-Agel, 2014; Ishihara and Qian, 2018). Further efforts have been made to capture more complex flow conditions, such as anisotropic wake growth in the cross-stream direction (Abkar and Porté-Agel, 2015; Gao et al., 2020), streamwise pressure gradients (Shamsoddin and Porté-Agel, 2018; Dar et al., 2023), and models based on the physical wake boundary (Ge et al., 2019). Models capable of capturing the effect of thermal stability and wind veer have been developed in recent years. The Gaussian model of Bastankhah and Porté-Agel (2014) has been modified to account for the effect of thermal stability (Abkar and Porté-Agel, 2015; Cheng et al., 2019; Dar et al., 2026). Similarly, Xiao et al. (2026) proposed a cosine model capable of capturing the effect of thermal stability on wake radius. Abkar et al. (2018) modified the Gaussian model (Bastankhah and Porté-Agel, 2014) in order to capture the effect of wind veer on the wake velocity deficit. They assumed the wind veer to be the same in the wake and ambient flow, and proposed a height-dependent lateral stretching of the wake. Although this assumption has been questioned in some studies (Churchfield and Sirnivas, 2018; Bodini et al., 2017; Englberger and Lundquist, 2020), it still serves as a reasonable approximation for the veer-related wake skewness. Narasimhan et al. (2024) also validated a model capable of capturing the effect of stable stratification and wind veer on the wake velocity deficit. All of the models discussed above use empirically obtained input parameters to relate the boundary layer flow conditions to the key wake characteristics, such as wake expansion and onset of the far wake. Some studies have shown that the performance of these models in a wide range of boundary layer conditions is significantly affected by the empirical input parameters (Krutova et al., 2020; Dar and Bachynski-Polić, 2026).

In order to limit the dependence of analytical models on empirical input parameters, Cheng and Porté-Agel (2018) proposed a physics-based model to estimate the wake expansion in a moderate to high turbulence neutral flow. Du et al. (2022) further extended this model to non-neutral conditions. Vahidi and Porté-Agel (2022) developed physics-based models for wake expansion and onset of the far wake under neutral flow ranging from low to high inflow turbulence. Using a slightly different approach, Ali et al. (2024) also derived a diffusion-based wake model and validated it under a range of turbulence intensity in neutral flow. More recently, Souaiby and Porté-Agel (2026) validated the model of Vahidi and Porté-Agel (2022) under different thermal stability conditions without any veer effects.

Different superposition methods have been proposed in the literature to combine the individual turbine wakes in order to obtain the wind farm wake. These methods differ in the choice of summation principle, either using a linear sum (Lissaman, 1979; Niayifar and Porté-Agel, 2016) or a squared sum (Katic et al., 1986; Voutsinas et al., 1990) approach. They also differ in the choice of reference inflow velocity for individual turbine wakes, either using the global inflow velocity (Lissaman, 1979; Katic et al., 1986) or using the local inflow velocity for a turbine in the wind farm (Voutsinas et al., 1990; Niayifar and Porté-Agel, 2016). Out of these superposition methods, the local linear sum approach generally performs better than the rest (Zong and Porté-Agel, 2020; Du et al., 2025). More sophisticated physics-based models for wake superposition have also been proposed recently (Zong and Porté-Agel, 2020; Bastankhah et al., 2021). Wind farm models tend to over-predict power, especially in large wind farm arrays (Archer et al., 2018; Souaiby and Porté-Agel, 2024). This can be related to the linear wake growth assumption, which does not hold in large wind farms (Souaiby and Porté-Agel, 2024). Finally, to model individual turbine wakes in a wind farm, the effect of wake-added turbulence intensity must be accounted for. This is usually done using

https://doi.org/10.5194/wes-2026-210
Preprint. Discussion started: 17 November 2026
© Author(s) 2026. CC BY 4.0 License.



eawe european academy of wind energy
Open Access WIND ENERGY SCIENCE DISCUSSIONS

95 empirical models for wake-added turbulence (see e.g., (Crespo and Hernández, 1996; Frandsen, 2007; Zehtabiyan-Rezaie et al., 2024; Dar et al., 2026)), and by computing an effective turbulence intensity experienced by a turbine within a wind farm (Niayifar and Porté-Agel, 2016; Souaiby and Porté-Agel, 2024).

Since most attempts to model wakes under thermal stability or veer effects are limited to single turbines, wind farm wake velocity deficit models capable of capturing these effects are currently lacking. The contribution of this study is two-fold: firstly,
100 we integrate the physics-based wake expansion model of Vahidi and Porté-Agel (2022) with the veered wake velocity deficit model of Abkar et al. (2018) for a single turbine wake. The integrated model is validated under a range of thermal stability and wind veer conditions. Here, it is worthwhile to note that, Souaiby and Porté-Agel (2026) used the original formulation of Vahidi and Porté-Agel (2022) and validated it under different thermal stability conditions without any wind veer effect. Secondly, we develop an analytical framework based on the validated single wake model to model the wake of a wind farm
105 under different thermal stability and veer conditions. We perform large eddy simulation (LES) of single and multiple turbine wakes, which are used to inform the development of the analytical framework, as well as to assess its performance. In addition, we also test the developed framework against open-access large-eddy simulation data of wind farm wakes in a conventionally neutral boundary layer and over a diurnal cycle from the Johns Hopkins University turbulence database (JHTDB) (Zhu et al., 2025; Xiao et al., 2025). The rest of the article is structured as follows: Section 2 presents the details of the LES setup and data,
110 the analytical framework is developed and presented in Section 3, validation of the analytical framework against LES data is performed in Section 4, and finally, some concluding remarks are given in Section 5.

2 Large eddy simulations

In this section, we provide an overview of the LES data used in the study. For simulations performed in this study, we document the simulation setup and description of the simulated cases. In addition, we also describe the LES data retrieved from the
115 JHTDB.

2.1 SOWFA simulations

Simulations are performed using the open-source Simulator fOr Wind Farm Applications-6 (SOWFA-6) LES code (NREL, 2025a), developed by the National Laboratory of the Rockies (NLR) in the United States. SOWFA-6 is built on OpenFOAM-6 (Foundation, 2018), and coupled with OpenFAST (NREL, 2025b) to simulate wake flow in the atmospheric boundary layer. It
120 solves the filtered incompressible Navier-Stokes, continuity, and potential temperature equations using a finite-volume method (Johlas et al., 2022; Mishra et al., 2024). The momentum equations incorporate the Coriolis force, and the Boussinesq approximation is used to account for buoyancy effects. The Deardorff-Lilly one-equation subgrid-scale model (Deardorff, 1980) with atmospheric stability-dependent turbulent Prandtl number (Moeng, 1984) is used to account for subgrid-scale turbulent stresses. The LES code has been validated and utilized in numerous studies under different atmospheric stability and turbine operating
125 conditions (e.g., (Churchfield et al., 2012, 2015; Ghaisas et al., 2017; Churchfield and Sirnivas, 2018; Martinez-Tossas et al.,

https://doi.org/10.5194/wes-2026-210
Preprint. Discussion started: 17 November 2026
© Author(s) 2026. CC BY 4.0 License.



eawe european academy of wind energy
Open Access WIND ENERGY SCIENCE DISCUSSIONS

2018; Doubrawa et al., 2018; Johlas et al., 2019; Ning et al., 2021; Johlas et al., 2022; Scott et al., 2023; Bastankhah et al., 2024; Mishra et al., 2024; Dammann et al., 2025)).

The simulations are carried out using a “precursor-successor" approach. Periodic boundary conditions are specified at the horizontal boundaries during the precursor simulations, whereas inflow/outflow conditions are specified in the upwind/downwind boundaries during the turbine simulations, with the inflow conditions prescribed by the precursor simulations, and zero normal gradients specified at the outflow boundary. The bottom surface is treated using the Schumann–Grotzbach formulation (Schumann, 1975), where the Monin-Obukhov similarity theory (Monin and Obukhov, 1954) is used to relate the friction velocity to the flow adjacent to the surface, aerodynamic surface roughness length z_0, and surface heat flux q_0. The potential temperature has zero gradient at the lower boundary. The upper boundary has a slip condition for velocity, and a fixed gradient equal to the free stratification lapse rate for potential temperature. A Rayleigh damping layer is applied at the top 30% of the domain to prevent flow oscillation due to gravity wave reflection from the upper boundary. The precursor simulations are initially run for about 6.5 to 8 hours until quasi-stationary conditions are achieved, after which inflow conditions are stored for 4600 seconds. The flow statistics of the precursor and turbine simulations are computed over the last hour of the simulations. The total simulation time and averaging time are comparable to those reported in previous studies (e.g., (Ghaisas et al., 2017; Johlas et al., 2022; Dammann et al., 2025)).

The ABL flow is driven by geostrophic wind, where nine different boundary layers corresponding to three conventionally neutral (CNBL), three stable, and three unstable simulations are simulated (Table 1). A latitude $\Phi = 65^\circ$ is specified to represent the Norwegian offshore conditions, and the wind speed and direction are set to be $U_h = 9\ \mathrm{m\,s^{-1}}$ and $\theta_h = 270^\circ$ at the turbine hub height. The domain is 8 km by 3 km in the streamwise and spanwise directions, respectively, in all simulations. The domain height is varied to enable different inversion heights in stable simulations. The grid resolution is 10 m in all directions in CNBL and unstable simulations, and it is 8 m in the horizontal directions and 5 m in the vertical direction in the stable simulations. The chosen grid resolution is comparable to previous studies (Ghaisas et al., 2017; Johlas et al., 2019; Bastankhah et al., 2024; Dammann et al., 2025). A capping inversion with a lapse rate of 0.03 $\mathrm{K\,m^{-1}}$ and a width of 100 m is defined at the top of the boundary layer, which is set at 700 m for the CNBL and unstable simulations, and 300 m for the stable simulation with a domain height of 500 m, and 500 m for two stable simulations with a domain height of 750 m. A stable free atmosphere stratification with a lapse rate of 0.003 $\mathrm{K\,m^{-1}}$ is applied above the capping inversion, and below the capping inversion, a constant potential temperature is initially specified for all simulations. An overview of key simulation parameters for all simulated boundary layers is given in Table 1.

The IEA 15 MW wind turbine (Gaertner et al., 2020) is used to simulate the wake flow. The turbine has a rotor diameter $D = 240$ m, and a hub height $z_h = 150$ m. The NREL reference open-source controller (ROSCO) (Abbas et al., 2022) is used to control the turbine. At each time step of the flow simulation, the velocity field information from the SOWFA-6 flow solver is passed to OpenFAST, which computes the unsteady forces on each blade, advances the blade rotation, and feeds the updated forces back to the flow solver. The turbine is modelled as bottom-fixed, and the rotor has a pre-cone angle of -4°, and a tilt angle of 6°. The turbine forces computed from OpenFAST are projected back on the flow domain on a circular disk centred

https://doi.org/10.5194/wes-2026-210
Preprint. Discussion started: 17 November 2026
© Author(s) 2026. CC BY 4.0 License.



eawe european academy of wind energy
Open Access WIND ENERGY SCIENCE DISCUSSIONS

Case	Domain Size ($x \times y \times z$) (km × km × km)	$N_x \times N_y \times N_z$	z_0 (m)	q_0 ($\mathrm{K\,m\,s^{-1}}$)	C_r K/hr	L_0 (m)	u_* ($\mathrm{m\,s^{-1}}$)
SOWFA-N1	$8 \times 3 \times 1$	$800 \times 300 \times 100$	0.0005	0	-	∞	0.25
SOWFA-N2			0.05				0.37
SOWFA-N3			0.5				0.49
SOWFA-U1			0.0005	0.02		-110	0.31
SOWFA-U2			0.05			-320	0.44
SOWFA-U3				0.08		-110	0.50
SOWFA-S1	$8 \times 3 \times 0.5$	$1000 \times 375 \times 100$	0.0005	-	-0.125	170	0.21
SOWFA-S2	$8 \times 3 \times 0.75$	$1000 \times 375 \times 150$	0.05			300	0.31
SOWFA-S3					-0.18	160	0.26

Table 1. Summary of key simulation parameters for different LES cases. x, y and z represent the streamwise, spanwise and vertical coordinates, N_x, N_y and N_z denote the number of grid points in respective directions, z_0 is the aerodynamic surface roughness length, q_0 is the surface heat flux, C_r is the cooling rate, L_0 is the surface Obukhov length (Stable: $0 < L_0(m) < 1000$, Unstable: $0 > L_0(m) > -1000$, Neutral: $L_0(m) > |1000|$), and u_* is the friction velocity.

at the hub height using a Gaussian Dirac delta function, with a projection width of 1.5 times the grid resolution (Revaz and Porté-Agel, 2021).

Single turbine wakes are simulated by placing the turbine 1.5 km (6.25 D) away from the inflow boundary in the middle of the domain span for all boundary layers listed in Table 1. In addition, a fully aligned turbine array comprising three turbines with a streamwise spacing of 7.5 D is also simulated for N1,2, U1,2, and S1,2 cases.

2.2 JHTDB simulations

The Johns Hopkins University turbulence database provides two wind farm datasets (JHU, 2026). The data retrieved from this database, along with a brief description of the simulation setup, are described here. For more details, the reader is referred to dedicated publications documenting the two datasets (Zhu et al., 2025; Xiao et al., 2025).

The first dataset (Zhu et al., 2025) simulates a large wind farm in a 10 × 6 array comprising NREL 5MW wind turbines, with a streamwise spacing of 7 D and spanwise spacing of 5 D. The turbines are parameterized using the actuator line method. Due to the periodic spanwise boundary conditions and the distance of the turbines from the spanwise walls, the wind farm is computationally infinite in the spanwise direction and can therefore be described as a semi-infinite wind farm with finite length and infinite span. The wind farm experiences a conventionally neutral boundary layer flow, with the latitude set to 43.44°.

The second dataset (Xiao et al., 2025) simulates a 4 × 2 wind farm also comprising NREL 5MW wind turbines in a diurnal cycle. The turbine parameterization and inter-turbine spacing are the same as in the other dataset. It is also a semi-infinite wind farm with infinite span, with the same latitude as the first dataset. For the sake of simplicity, the wind farm direction is fixed and does not necessarily follow the change in the wind direction of the incoming boundary layer over the diurnal cycle. For

https://doi.org/10.5194/wes-2026-210
Preprint. Discussion started: 17 November 2026
© Author(s) 2026. CC BY 4.0 License.



the purpose of the current study, we computed hourly averages at selected times: (i) 12:00:00-13:00:00 (noon), (ii) 15:00:00 - 16:00:00 (early afternoon), (iii) 18:00:00 - 19:00:00 (late afternoon), (iv) 22:00:00 - 23:00:00 (evening), and (v) 05:00:00 - 06:00:00 (early morning).

2.3 Overview of LES data

We now present an overview of the LES data to give an insight into the wide range of flow conditions tested in this study. Figure 1 compares key boundary layer characteristics between the SOWFA precursor simulations. The time- and horizontally-averaged normalized streamwise and spanwise velocity components together with the resulting vertical wind veer are first discussed (presented in Figure 1 (a-c)). For the sake of brevity, the terms streamwise or spanwise velocity (or velocity deficit) will refer to the normalized averaged (time- and span-averaged in the boundary layer flow, and only time-averaged in the wake flow) streamwise or spanwise velocity (or velocity deficit) throughout the article, unless otherwise stated.

The three CNBL cases show an increase in the mean flow shear in the streamwise velocity profile with an increase in the surface roughness, whereas the spanwise velocity profiles are comparable for all CNBL cases. For the unstable cases, the mean flow shear in the streamwise velocity is smaller than in the CNBL ones due to higher turbulent mixing, which is also observed to increase with the increase in the surface roughness. The spanwise velocity also shows an approximately constant value in the vertical direction for different unstable cases. For the stable cases, a low-level jet (LLJ) can be observed in the streamwise velocity profiles. The location of the low-level jet varies between cases. Near the surface, the stable cases also show a higher mean flow shear compared to the unstable and CNBL cases. The spanwise velocity has the highest magnitude in the stable cases compared to the CNBL and unstable cases, with comparable values within different stable cases. The resulting vertical wind veer depends on the stability class, with the stable cases showing the highest magnitude of wind veer ($\approx 20°$) across the rotor, followed by CNBL cases ($\approx 8°$), whereas the unstable cases show negligible veer ($< 0.5°$), however, in some unstable cases (SOWFA-U2,3), the hub height wind direction is offset from zero to $\approx 2°$.

The turbulence characteristics in different boundary layers are compared in Figure 1 (d-g). For a given surface roughness, an unstable boundary layer shows higher turbulence levels, and a stable one shows lower turbulence compared to the CNBL case. Similarly, the turbulence level increases (decreases) with an increase in the strength of stability for the unstable (stable) cases. There are certain cases that show comparable normalized turbulence kinetic energy (TKE) between different stability conditions: SOWFA-N3 and SOWFA-U2; SOWFA-N2 and SOWFA-U1; and SOWFA-N1 and SOWFA-S3 show comparable TKE over the turbine rotor. However, even for the cases that show comparable TKE levels, the turbulence intensity components show a different vertical structure (especially the vertical turbulence intensity in the unstable and CNBL cases), indicating that the distribution of turbulence over different components is still different. The overall range of turbulence at hub height is quite wide: 2.3% - 4.3% in the stable cases, 3.5% - 8.75% in the CNBL cases, and 4.5% - 11% in the unstable cases. Finally, the potential temperature profiles are also shown in Figure 1 (h). The stable cases show a linear increase in the potential temperature with height over the rotor, the unstable cases show a sharp negative gradient near the surface with a constant profile over the rotor (attributed to high turbulent mixing), whereas the CNBL cases show a constant potential temperature

https://doi.org/10.5194/wes-2026-210
Preprint. Discussion started: 17 November 2026
© Author(s) 2026. CC BY 4.0 License.

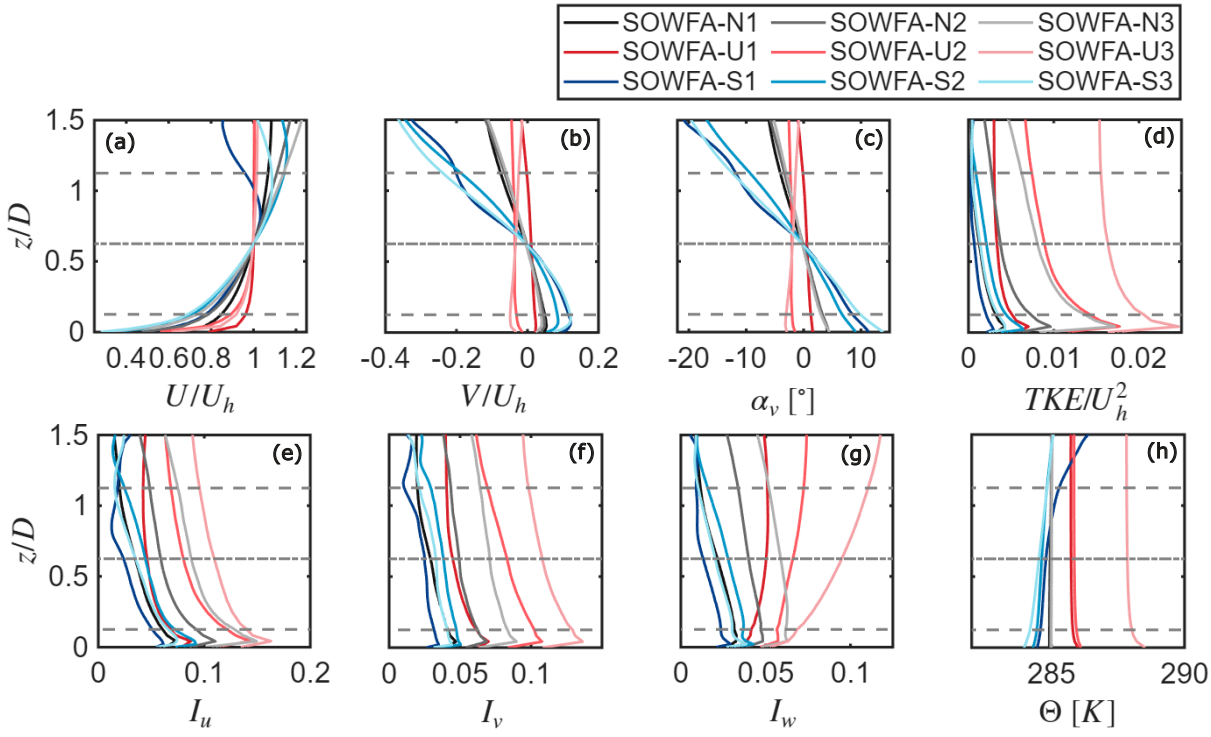


Figure 1. Vertical profiles of time and horizontally averaged boundary layer characteristics in the precursor simulations: normalized streamwise velocity (a), normalized spanwise velocity (b), vertical wind veer (c), normalized turbulence kinetic energy (d), streamwise, spanwise and vertical turbulence intensity (e-g), and (h) potential temperature. The grey horizontal dashed dotted line represents the prospective turbine hub height ($0.625D$), whereas the grey horizontal dashed lines show the rotor top and bottom tip heights.

profile. The observed boundary layer characteristics are generally consistent with those reported in the previous studies (see e.g., (Wu et al., 2024; Dar et al., 2026; Xie and Archer, 2017; Narasimhan et al., 2024; Abkar and Porté-Agel, 2015)).

In addition to the boundary layer characteristics, we also provide an overview of the wake simulations in SOWFA because the single-wake data are used to inform the development of the analytical modelling framework. Figure 2 shows the streamwise velocity contours in a cross-stream plane at selected downstream locations for all single turbine simulations. The stable cases show a highly skewed wake shape due to the veer effect. The interaction between the LLJ and the turbine wake can also be observed. The nature of this interaction is dependent on the position of the LLJ relative to the rotor (Doosttalab et al., 2020; Gadde and Stevens, 2021). The CNBL cases also show a skewed wake shape, however, the degree of skewness is smaller compared to the stable cases due to the smaller magnitude of veer in these cases. Finally, the unstable cases show a relatively axisymmetric wake shape, with a considerably faster recovery compared to the CNBL and stable cases.

To further characterize the wake, we compute the streamwise wake velocity deficit $\Delta U = U_{nw} - U_w$, where U_{nw} is the boundary layer streamwise velocity and U_w is the streamwise velocity in the wake, respectively. Figure 3 compares the maximum normalized wake velocity deficit for the single wake cases. In the CNBL cases, an increase in the turbulence level in the incoming boundary layer leads to a faster recovery of the maximum wake deficit, which is consistent with previous ob-

https://doi.org/10.5194/wes-2026-210
Preprint. Discussion started: 17 November 2026
© Author(s) 2026. CC BY 4.0 License.

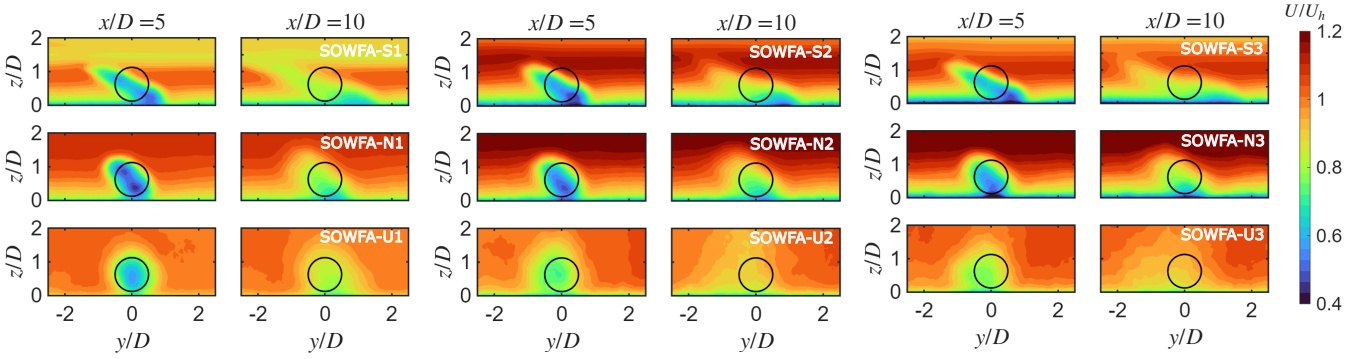


Figure 2. Cross-stream contours of the normalized averaged streamwise velocity for a single turbine wake in different cases. The black circles show the rotor outline.

servations (Porté-Agel et al., 2020). The unstable cases show a faster wake recovery compared to the CNBL cases, even for the cases with comparable TKE levels. This is consistent with the findings of Du et al. (2021). Comparing SOWFA-U1 and SOWFA-U2 cases, the latter has weaker stability strength, however, it has a significantly higher surface roughness, which leads to significantly higher turbulence levels and a faster recovery than the former. For the SOWFA-U3 case, the stability strength is comparable to the SOWFA-U1 case, and the surface conditions are the same as SOWFA-U2 case, which leads to higher turbulence levels and the fastest recovery of the maximum wake deficit of all the cases. The stable cases are more interesting, as these depict comparable behaviour of the maximum wake deficit and show a faster recovery of the deficit compared to the CNBL cases, which is contrary to the usual observation of the slower recovery under stable cases compared to neutral ones (as reported in e.g., (Abkar and Porté-Agel, 2015; Du et al., 2021; Dar et al., 2026)). This can be explained by the interaction of the LLJ with the turbine wake. As discussed in previous studies (Doosttalab et al., 2020; Gadde and Stevens, 2021), an LLJ location in the upper half of the rotor or slightly above the top tip level leads to the development of an unstable shear layer, which enhances entrainment of higher energy flow from the LLJ to the lower energy wind turbine wake, leading to a faster recovery of the wake compared to the CNBL cases.

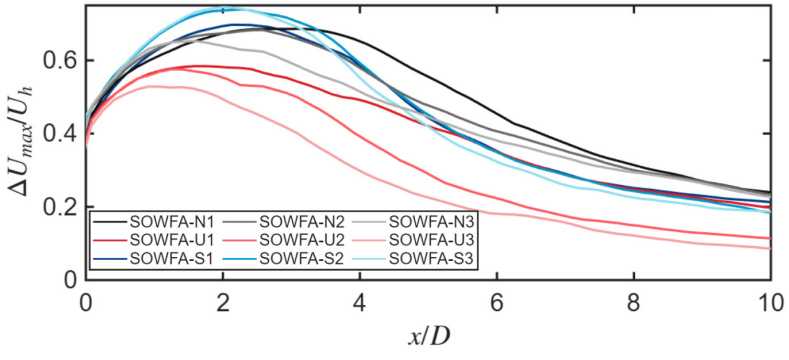


Figure 3. Comparison of maximum normalized averaged streamwise velocity deficit for a single turbine.

https://doi.org/10.5194/wes-2026-210
Preprint. Discussion started: 17 November 2026
© Author(s) 2026. CC BY 4.0 License.



eawe european academy of wind energy
Open Access WIND ENERGY SCIENCE DISCUSSIONS

Finally, we present an overview of different boundary layer characteristics in the LES simulations from JHTDB used for validation later in the study. Figure 4 (a-c) compares the time- and spanwise-averaged streamwise and spanwise velocity components, as well as the resulting wind veer. The CNBL case shows a sheared streamwise velocity profile, with very small spanwise velocity and resulting wind veer, which can be attributed to the smaller latitude and higher boundary layer height compared to the SOWFA simulations. For the diurnal cycle simulations, we picked several representative times to test the model. During daytime, the boundary layer is mostly unstable, as a result, the noon and early afternoon boundary layers show higher shear close to the ground and approximately constant streamwise velocity across the rotor. The spanwise velocity shows very small veer, however, at noon the wind direction is approximately 11° at the hub height. In the late afternoon, the boundary layer usually transitions from the unstable to stable regime (Abkar et al., 2016), which is consistent with a higher shear in the streamwise velocity profile and a constant wind direction at around -11° - characteristics that partly resemble the stable and unstable boundary layers. The evening and early morning boundary layers are characterized by high shear and veer - characteristics of highly stable boundary layers. The magnitude of veer over the rotor is significantly higher than the SOWFA stable simulations. In the early morning, a low-level jet can also be observed with a peak slightly below the rotor top tip. It is to be noted that, the wind turbines are not aligned with the wind direction in these cases; as a consequence, the noon and late afternoon cases produce wake deflection, resulting in partial wake conditions for downstream turbines in the farm (Xiao et al., 2025).

A comparison of turbulence intensity components between different test cases is also shown in Figure 4 (d-f). The CNBL and daytime boundary layers show comparable turbulence intensity profiles, while the evening and early morning boundary layers show significantly lower turbulence.

Overall, both the SOWFA cases and the cases selected from the JHTDB show a diverse range of boundary layer characteristics such as, mean flow shear, turbulence levels, wind veer magnitude, low-level jets, and thermal stability. In addition, the turbine types and wind farm configurations also vary between different cases.

3 Analytical modelling framework

The analytical framework for modelling the wind farm wake velocity deficit is developed and presented in this section. The overall approach to model the wind farm wake is similar to previous studies (Niayifar and Porté-Agel, 2016; Souaiby and Porté-Agel, 2024): the wake velocity deficit of each turbine is individually modelled, following which a superposition method is used to combine the wakes of all turbines in a wind farm to yield the cumulative wake velocity deficit. Therefore, the modelling framework has two key components: an analytical wake model for the velocity deficit of a stand-alone turbine, and a superposition principle to combine wakes from individual turbines into one. In modelling the individual wake deficit of turbines experiencing a waked inflow, the effect of upstream turbine wakes is accounted for by their influence on input parameters for the analytical wake model, such as the altered turbulence characteristics within a wind farm compared to the boundary layer flow.

https://doi.org/10.5194/wes-2026-210
Preprint. Discussion started: 17 November 2026
© Author(s) 2026. CC BY 4.0 License.

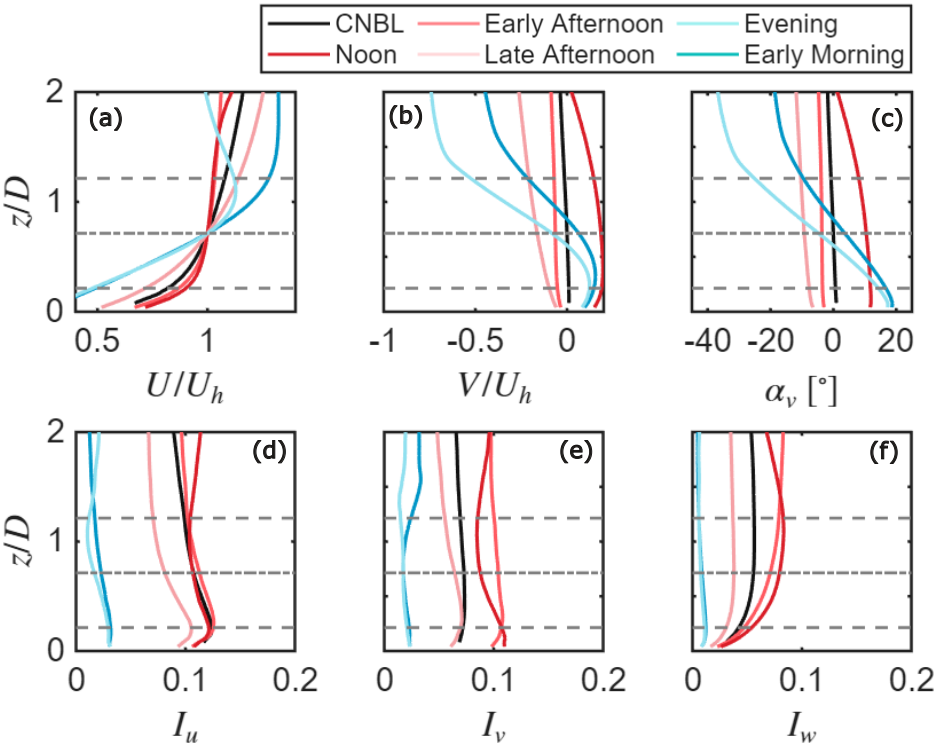


Figure 4. Vertical profiles of time- and spanwise-averaged boundary layer characteristics in the precursor simulations from JHTDB: normalized streamwise velocity (a), normalized spanwise velocity (b), vertical wind veer (c), streamwise, spanwise and vertical turbulence intensity (d-f). The grey horizontal dashed dotted line represents the prospective turbine hub height, whereas the grey horizontal dashed lines show the rotor top and bottom tip heights.

In the following, we will first present the stand-alone analytical wake model, followed by the additional considerations to properly model the individual velocity deficit of waked turbines, and finally, the superposition method used in the study. In addition, a reference model used for the sake of benchmarking is also presented.

3.1 Stand-alone wake model

The wake velocity deficit behind a wind turbine can be expressed as (Porté-Agel et al., 2020; Dar and Bachynski-Polić, 2026):

$$\frac{\Delta U}{U_h} = C(x) f(x, y, z, \sigma(x)), \tag{1}$$

where $C(x)$ is the normalized maximum wake velocity deficit, $f(x, y, z, \sigma(x))$ is the shape function for the cross-stream velocity deficit distribution at a given streamwise location, and σ is the wake width in the cross-stream direction taken as the geometric mean of the spanwise and vertical wake widths ($\sigma = \sqrt{\sigma_y \sigma_z}$, with σ_y and σ_z as the spanwise and vertical wake width, respectively).

https://doi.org/10.5194/wes-2026-210
Preprint. Discussion started: 17 November 2026
© Author(s) 2026. CC BY 4.0 License.



eawe european academy of wind energy
Open Access WIND ENERGY SCIENCE DISCUSSIONS

The wake model used in the study combines the models of Abkar et al. (2018) and Vahidi and Porté-Agel (2022). Abkar et al. (2018) proposed a modification to the Gaussian model of Bastankhah and Porté-Agel (2014) to account for the effect of wind veer on the wake velocity deficit. Vahidi and Porté-Agel (2022), on the other hand, proposed a physics-based model to compute the wake width, which was inspired by the Taylor diffusion theory, and accounted for the effect of temporal coherence of large turbulent eddies (by using integral timescales), and wake diffusion due to velocity fluctuations (by using turbulence intensity) on the cross-stream expansion of the wake. They used a super-Gaussian wake shape in the near-wake, and a Gaussian one in the far-wake. This model also eliminates the need for empirical relations (like the ones assessed by Dar and Bachynski-Polić (2026)) to estimate the wake expansion rate and width. In the following, we integrate the model of Abkar et al. (2018) within the model of Vahidi and Porté-Agel (2022) to develop a physics-based veer- and thermal stability-dependent wake model. The model equations are presented in the sequence of implementation. For more details on the derivations of the model equations, the reader is referred to the original articles (Vahidi and Porté-Agel, 2022; Abkar et al., 2018).

The wake behind the turbine is divided into three distinct regions: (i) the expansion region, (ii) the near-wake region, and (iii) the far-wake region. The model presented in the following is applicable from the end of the expansion region to any desired downstream location.

The length of the near-wake region x_{nw} is first estimated as:

$$\frac{x_{nw}}{D} = \frac{\sigma_{e,nw}}{D} \frac{1+\sqrt{1-C_T}}{2(\sqrt{Sc_t I_v I_w} + S'(1-\sqrt{1-C_T}))} + \frac{x_0}{D}, \tag{2}$$

where $\sigma_{e,nw}$ is the mixing layer characteristic length at the end of the near-wake region, C_T is the turbine thrust coefficient, Sc_t is the turbulent Schmidt number, $I_{v,w}$ are the spanwise and vertical turbulence intensity values at the turbine hub height, respectively, S' is the spreading rate of the mixing layer, and x_0 is the length of the expansion region. Following Vahidi and Porté-Agel (2022), we set $\sigma_{e,nw} = 0.18D$, $Sc_t = 0.5$, and $x_0 = D$ for a turbine in the free-flow. Vahidi and Porté-Agel (2022) proposed a spreading rate $S' = 0.043$. In the current work, we adopt this value for all cases except those involving the low-level jets. As explained in previous studies (Doosttalab et al., 2020; Gadde and Stevens, 2021), the presence of the LLJ leads to an unstable mixing (shear) layer, which leads to a faster entrainment of energy from the outer flow to the wake flow. This is consistent with a higher spreading rate of the mixing layer. Therefore, we set $S' = 0.07$ for a turbine experiencing the LLJ in the current study. The value is chosen as the best fit to the SOWFA simulations.The value(s) chosen for S' may not be universal, and further research is needed to determine its sensitivity to atmospheric and turbine operating conditions.

In the far-wake region ($x > x_{nw}$), the wake centre velocity U_{centre} is expressed as (Bastankhah and Porté-Agel, 2014):

$$C(x) = \frac{U_{centre(x)}}{U_h} = \sqrt{1 - \frac{C_T}{8\left(\frac{\sigma(x)}{D}\right)^2}}. \tag{3}$$

A streamwise-marching iterative procedure is applied to estimate U_{centre} and σ. The value for U_{centre} is initialized from the closest upstream location, where it is set from the one-dimensional momentum theory at the start of the far-wake. At each downstream location, the travel time of the wake is computed as:

https://doi.org/10.5194/wes-2026-210
Preprint. Discussion started: 17 November 2026
© Author(s) 2026. CC BY 4.0 License.



eawe european academy of wind energy
Open Access WIND ENERGY SCIENCE DISCUSSIONS

$$T = \int_{x_0}^{x} \frac{1}{U_a(x)} dx, \tag{4}$$

where U_a is the advection velocity given as $U_a(x) = 0.5(U_h + U_{centre}(x))$.

Following this, the spanwise mixing layer characteristic length is estimated as:

$$\sigma_{e,y}(x) = \sqrt{Sc_t}\sigma_v T_v^L \sqrt{2\left[\frac{T}{T_v^L} - \left(1 - \exp\left(-\frac{T}{T_v^L}\right)\right)\right]} + 2S'(U_h T - (x - x_0)), \tag{5}$$

where σ_v is the standard deviation in the spanwise velocity at the turbine hub height, and T_v^L is the Lagrangian spanwise integral timescale at the turbine hub height. The first term in the above equation represents the contribution of the ambient turbulence to the mixing layer characteristic length, and the second term is the contribution of the turbine-induced wake spreading. The spanwise mixing layer characteristic length is then related to the spanwise wake width by the following relation:

$$\frac{\sigma_y}{\sigma e, y} = 1.95\exp(-6.19\frac{\sigma_{e,y}}{D}) + 10.96\exp(-20.05\frac{\sigma_{e,y}}{D}) + 1.03. \tag{6}$$

Equations 5 and 6 are then applied to obtain $\sigma_{e,z}$ and σ_z (by replacing σ_v with σ_w and T_v^L with T_w^L), respectively. Following Vahidi and Porté-Agel (2022), the Lagrangian integral timescale can be determined from the Eulerian one (T^E) as:

$$T^L = \frac{0.7T^E}{I}, \tag{7}$$

where I can be I_v for the spanwise timescale or I_w for the vertical one.

Once the total wake width ($\sigma = \sqrt{\sigma_y \sigma_z}$) is obtained, the values for U_{centre}, U_a and T are updated. The procedure is repeated until convergence by iterating over equations 3 - 6 for all streamwise locations.

Once the wake centre velocity and wake width has been computed, the wake deficit profile can be expressed following Abkar et al. (2018):

$$\frac{\Delta U}{U_h} = \left(1 - \sqrt{1 - \frac{C_T}{8\left(\frac{\sigma}{D}\right)^2}}\right) \exp\left[-\frac{1}{2}\left(\frac{(y + \Delta y(x,z))^2}{\sigma_y(x)^2} + \frac{(z - z_h)^2}{\sigma_z(x)^2}\right)\right], \tag{8}$$

where Δy is the skew in the wake shape due to wind veer. The wake skew due to veer can be determined as:

$$\Delta y(x,z) = x\ \tan(c_1 \alpha_v(z) + c_2), \tag{9}$$

https://doi.org/10.5194/wes-2026-210
Preprint. Discussion started: 17 November 2026
© Author(s) 2026. CC BY 4.0 License.



eawe european academy of wind energy
Open Access WIND ENERGY SCIENCE DISCUSSIONS

where α_v is the wind veer in the boundary layer flow. The above equation is different from the one defined by Abkar et al. (2018). While Abkar et al. (2018) assumed that the veer effect is the same between the boundary layer and wake flow, others (Churchfield and Sirnivas, 2018; Englberger and Lundquist, 2020) reported that the wake veer is usually smaller than the one in the boundary layer flow. In Equation 9, we propose a correction to the wake skew due to wind veer, accounting for the difference in the wake and boundary layer veer. Using the SOWFA LES data reported by Englberger and Lundquist (2020), we defined a linear relationship between the wake and boundary layer veer, where $c_1 = 0.7966$ and $c_2 = 0.0584$.

In the near-wake region ($x < x_{nw}$), the wake is assumed to be skewed super-Gaussian:

$$\frac{\Delta U}{U_h} = \left(1 - \sqrt{1 - C_T}\right) \exp\left(-\frac{r^{n(x)}}{2\sigma'^2(x)}\right), \tag{10}$$

where r is the distance from the wake centre, which for a skewed wake can be expressed as:

$$r = \sqrt{(y + \Delta y)^2 + (z - z_h)^2}, \tag{11}$$

n is the smoothness parameter given by Vahidi and Porté-Agel (2022):

$$n(x) = 2 + 12\,\mathrm{erfc}\left(\frac{2\sigma_e(x)/D}{0.18}\right), \tag{12}$$

and σ' is the super-Gaussian wake width computed by:

$$\sigma'(x) = \left[\frac{n(x)C_T}{2^{2/n(x)}(1 - \sqrt{1 - C_T}) - (1 - \sqrt{1 - C_T})^2} \frac{1}{16\Gamma(2/n(x))}\right]^{n(x)/4}, \tag{13}$$

where Γ is the Gamma function.

3.2 Waked turbine considerations

To compute the individual wakes of waked turbines, the effect of upstream turbines on the inflow experienced by these turbines must be accounted for. This is done by modifying key inputs for the wake model, as described in this section. The updated input parameters accounting for waked inflow are then used in the stand-alone wake model to compute individual wake velocity deficit of waked turbines.

3.2.1 Expansion region length and spreading rate

As discussed by Souaiby and Porté-Agel (2024), the length of the expansion region is reduced in waked inflow conditions. They proposed a value of $x_0 = 0.5D$ for waked conditions. Following them, we also adopt the same value for the length of the expansion region, without any specific calibration on our data.

https://doi.org/10.5194/wes-2026-210
Preprint. Discussion started: 17 November 2026
© Author(s) 2026. CC BY 4.0 License.



eawe european academy of wind energy
Open Access WIND ENERGY SCIENCE DISCUSSIONS

In addition, we use the same spreading rate $S' = 0.043$ for all flow conditions for waked turbines. This can be understood as follows: for the turbines experiencing an LLJ, the front-row turbines are most affected by the LLJ-induced faster mixing layer growth, whereas the downstream turbines do not experience an LLJ, which can also be seen in Figure 2. As a result, the original value for S' from Vahidi and Porté-Agel (2022) is adopted for all waked flow conditions.

3.2.2 Turbine-modified integral timescales

As a wind turbine interacts with the boundary layer, it modulates the large-scale turbulent eddies in the flow. As a result, the integral timescales in the wake flow are affected by the turbine rotor. Several studies have investigated the streamwise integral time or length scales in the wake of stand-alone turbine and wind farm configurations (Chamorro et al., 2013; Jin et al., 2016; Liu et al., 2018, 2022). The main findings from these studies are as follows: the integral scales in the wake evolve on the order of the rotor radius; and within a wind farm with a typical turbine spacing of 5 to 10 rotor diameters, the integral timescales remain approximately constant.

Following these studies, we plot the normalized Eulerian integral timescales in the spanwise and vertical velocities for single and array turbine cases in Figure 5. The characteristic timescale of the turbine based on the hub height velocity and rotor diameter is used for normalization. A wide range of inflow boundary layer normalized integral timescales can be seen in different cases, ranging from 0.15 to 3.2. Interestingly, the inflow integral timescale in both spanwise and vertical directions is smaller than 1 in all neutral and stable cases. This can be related to the large rotor diameter of the turbine considered in this study. The unstable cases show inflow timescales close to or above 1 in different turbulence levels. Even though the inflow timescales show a large variation between different cases, they are observed to fall within a smaller range in the wake of a wind turbine (see Figure 5 (a,c)). For instance, at $x/D = 5$, both spanwise and vertical normalized integral timescales range between 0.2 and 0.6 for all cases. This indicates that the turbine-induced scales dominate the wake flow, and is consistent with previous observations (Chamorro et al., 2013; Jin et al., 2016). Moreover, we can also see that within the turbine array, the value of both normalized integral timescales remains approximately constant (see Figure 5 (b,d)), which is also consistent with previous observations (Liu et al., 2018). This confirms that the observations of previous studies (Chamorro et al., 2013; Jin et al., 2016; Liu et al., 2018) hold in non-neutral conditions, and can be extended to cross-stream integral timescales.

Based on the above discussion, the cross-stream Eulerian integral timescales are assumed to be $T^E_{v(w)} = \frac{D}{2U_{in}}$ for the waked turbines, where U_{in} is the inflow velocity to a waked turbine. Once the Eulerian timescales are computed, they can be converted into the Lagrangian ones using Equation 7. It is to be noted that this is an approximation, as the actual integral timescales in the wake are on the order of the rotor radius and inflow velocity. As discussed by Souaiby and Porté-Agel (2026), the model of Vahidi and Porté-Agel (2022) can yield reasonable results as long as the order of the integral timescales is correctly estimated.

3.2.3 Wake-added turbulence intensity

Turbines exposed to wakes experience higher turbulence levels due to the wake-added turbulence intensity. Several models have been proposed to predict the streamwise wake-added turbulence intensity, ranging from one-dimensional models (Crespo and Hernández, 1996; Frandsen, 2007; Zehtabiyan-Rezaie et al., 2024) to three-dimensional ones (Ishihara and Qian, 2018;

https://doi.org/10.5194/wes-2026-210
Preprint. Discussion started: 17 November 2026
© Author(s) 2026. CC BY 4.0 License.

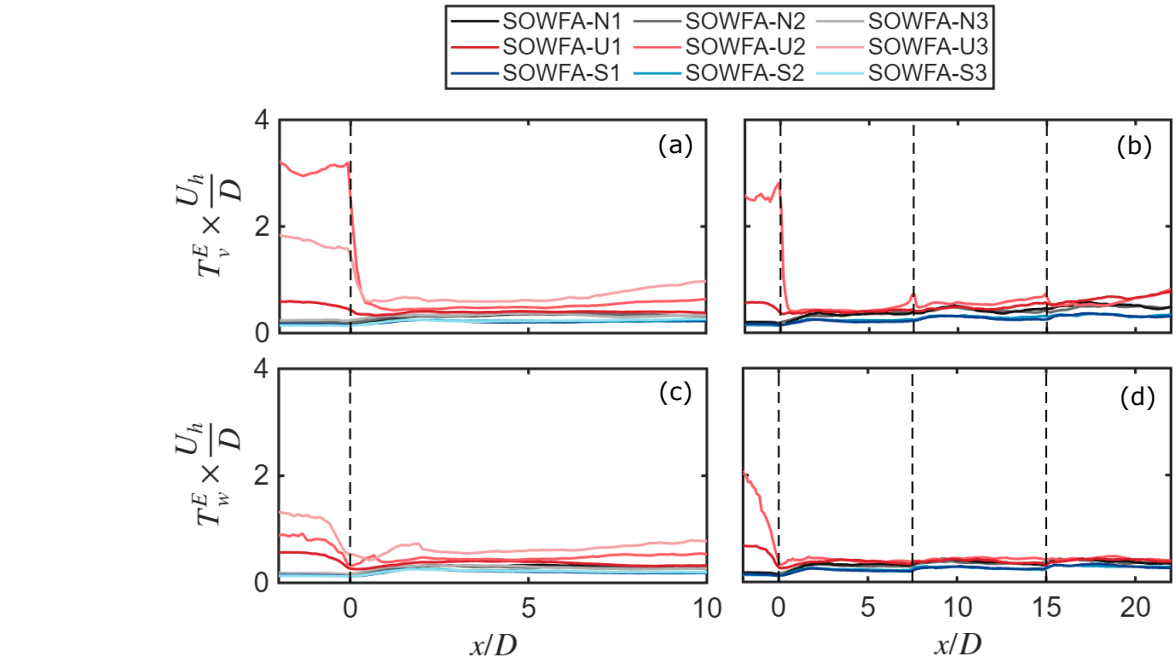


Figure 5. Normalized Eulerian integral timescales in the single (a,c) and array (b,d) cases at the hub height. The black dashed vertical lines show turbine locations.

Tian et al., 2022; Li et al., 2022). For analytical wind farm wake velocity models, one-dimensional wake-added turbulence models are commonly used, due to their simplicity and sufficient accuracy (Niayifar and Porté-Agel, 2016; Souaiby and Porté-Agel, 2024; Zehtabiyan-Rezaie et al., 2024). In this study, however, we need to estimate cross-stream wake-added turbulence components. More recently, Dar et al. (2026) proposed a modification to the Frandsen model (Frandsen, 2007) to estimate vertical wake-added turbulence intensity. However, similar to the Frandsen model, their model does not account for differences in ambient turbulence intensity and was calibrated on a single dataset under neutral conditions.

Due to the lack of appropriate models, we propose rotor-averaged wake-added turbulence models for spanwise and vertical components. The proposed models are modifications to the Crespo model (Crespo and Hernández, 1996), and expressed as:

$$I_a^v = p_1 a_T^{0.8325} I_{v,in}^{p_2} \left(\frac{x}{D}\right)^{p_3}, \tag{14}$$

$$I_a^w = s_1 a_T^{0.8325} I_{w,in}^{s_2} \left(\frac{x}{D}\right)^{s_3}, \tag{15}$$

where I_a^v and I_a^w are wake-added turbulence intensity components in the spanwise and vertical directions, respectively, a_T is the turbine induction factor, and $I_{v,in}$ ($I_{w,in}$) is the inflow spanwise (vertical) turbulence intensity. While we keep the exponent

https://doi.org/10.5194/wes-2026-210
Preprint. Discussion started: 17 November 2026
© Author(s) 2026. CC BY 4.0 License.



eawe european academy of wind energy
Open Access WIND ENERGY SCIENCE DISCUSSIONS

for the turbine induction factor the same as the original Crespo model, the rest of the exponents (p_1, p_2, p_3 for I_a^v, and s_1, s_2, s_3 for I_a^w) are calibrated. We use the single turbine SOWFA-N1,N2,S1,S2,U1,U2 cases for fitting the exponents of equations 14 and 15, whereas the SOWFA-N3,S3,U3 cases are used to test the model. The resulting exponents are listed in Table 2.

p_1	p_2	p_3	s_1	s_2	s_3
0.2878	-0.2049	-0.3793	0.4658	-0.1655	-0.6088

Table 2. Values of exponents in equation 14 and 15.

Figure 6 shows the comparison between the LES data and the model predictions. It can be seen that the model can predict the rotor averaged spanwise and vertical wake-added turbulence intensities with reasonable accuracy. There is also no significant drop in model accuracy between the cases used to fit the model and the ones used to test it.

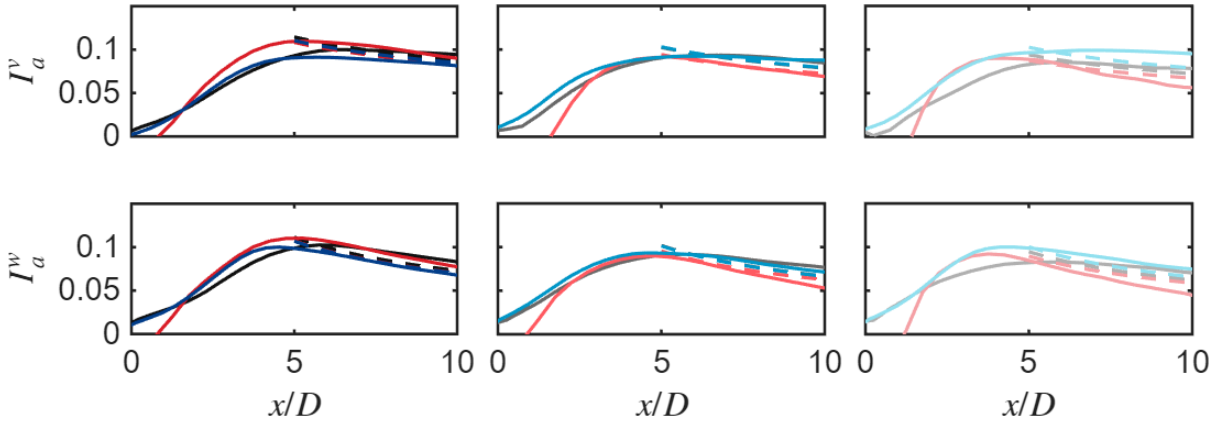


Figure 6. Rotor-averaged wake-added spanwise and vertical turbulence intensity in the single turbine wake. The solid lines show LES results and dashed lines show model predictions. The colour legend is same as Figure 5.

3.3 Wake superposition principles

Once the individual wake velocity deficit of different turbines in a wind farm has been computed, a superposition principle is applied to compute the total wake velocity deficit of the wind farm. In this work, we use the local linear summation approach proposed by Niayifar and Porté-Agel (2016). According to this approach, the total wake velocity over the wind farm can be computed as:

$$U(x,y,z) = U_h - \sum_i (U_i - U_{wi}(x,y,z)), \tag{16}$$

where U is the total wind farm wake velocity, U_i is the inflow velocity experience by a turbine i, and U_{wi} is the wake velocity of turbine i.

https://doi.org/10.5194/wes-2026-210
Preprint. Discussion started: 17 November 2026
© Author(s) 2026. CC BY 4.0 License.



eawe european academy of wind energy
Open Access WIND ENERGY SCIENCE DISCUSSIONS

In addition to the superposition of the wake velocity, a superposition strategy to compute total turbulence intensity experienced by a waked turbine is also needed. Different methods have been proposed in the literature to compute the total turbulence intensity in the wake, ranging from considering only the impact of the closest upstream turbine (Niayifar and Porté-Agel, 2016; Zehtabiyan-Rezaie et al., 2024) to considering the impact of all upstream turbines (Li et al., 2023). Souaiby and Porté-Agel (2024) assessed different superposition strategies for the turbulence intensity in the wake for a range of wind farm configurations. They found that the strategy based on cumulative added turbulence of all upstream turbines while accounting for local inflow velocity changes performed the best. Therefore, following them, we also adopt this strategy, which can be stated as follows:

$$I_{vj} = \sqrt{\left(I_{v,in}\frac{U_h}{U_j}\right)^2 + \sum_k \left(\frac{A_w}{A_R} I^v_{a,kj} \frac{U_k}{U_j}\right)^2}, \tag{17}$$

where I_{vj} is the total spanwise turbulence intensity experienced by turbine j in the wind farm, $I^v_{a,kj}$ is the added spanwise turbulence intensity at turbine j due to an upstream turbine k, U_k and U_j are the inflow velocities at the respective turbines, A_R is the rotor area, and A_w is the intersection between the wake area of an upstream turbine k at turbine j and the rotor area. Following Niayifar and Porté-Agel (2016), the wake area is computed as 4σ. The total vertical turbulence intensity is computed following the same approach.

3.4 Estimation of key input parameters

In the modelling framework detailed above, there are five key input parameters: the turbine thrust coefficient, the spanwise and vertical Lagrangian integral timescales, and the spanwise and vertical turbulence intensity components. While the turbine thrust coefficient can be obtained from manufacturer-provided performance curves for a certain turbine, the other inputs need quantification of the inflow boundary layer. One approach to obtain the spanwise and vertical integral timescales and turbulence intensities is through direct measurements at a characteristic height, such as the turbine hub height. Following this approach, we will obtain input parameters from the precursor simulations to characterize the inflow boundary layer. This approach will be referred to as 'Model-v1' in the rest of the paper.

Alternatively, one can use empirical relations to obtain these parameters based on the site and flow conditions. This can be especially relevant in scenarios where direct measurements of cross-stream turbulence intensities or integral timescales in the boundary layer flow are unavailable. In the following, we propose a framework based on empirical relations proposed in the literature to obtain the input parameters for the model. The streamwise turbulence intensity at the hub height can be obtained using the relation proposed by Narasimhan et al. (2024):

$$I_u = [-A_1 \log\left(\frac{z_h}{\delta}\right) + B_1]^{\frac{1}{2}} \left(\frac{u_*}{U_h}\right), \tag{18}$$

https://doi.org/10.5194/wes-2026-210
Preprint. Discussion started: 17 November 2026
© Author(s) 2026. CC BY 4.0 License.



eawe european academy of wind energy
Open Access WIND ENERGY SCIENCE DISCUSSIONS

where $A_1 = 1.25$ and $B_1 = 0.6$ are empirical constants based on previous works (Hultmark et al., 2012; Meneveau and Marusic, 2013; Narasimhan et al., 2024), and δ is the boundary layer height. The spanwise and vertical ones can then be obtained following the suggestions from Cheng et al. (2019):

$$I_v = I_u \left(1 - 0.22\cos^4\left(\frac{\pi z_h}{2\delta}\right)\right), \tag{19}$$

$$I_w = I_u \left(1 - 0.45\cos^4\left(\frac{\pi z_h}{2\delta}\right)\right). \tag{20}$$

In the above equations, the boundary layer height is estimated as (Cheng et al., 2019):

$$\delta = \frac{u_*}{6f}, \tag{21}$$

where f is the Coriolis force computed by the following equation:

$$f = 2\Omega\sin(\phi), \tag{22}$$

where Ω is the angular speed of the Earth ($\Omega = 72.9 \times 10^{-6}$ rad s^{-1}), and ϕ is the latitude of the site.

Once the turbulence intensity components have been estimated, these can be further used to estimate the Lagrangian integral timescales. Souaiby and Porté-Agel (2026) used the empirical relations proposed by Hanna (1984) to estimate the Lagrangian integral timescales. These are given as follows:

$$T_v^L = \begin{cases} 0.5\frac{z_h}{\sigma_w}, \text{ Neutral} \\ \left(\frac{0.07\delta}{\sigma_v}\right)\sqrt{\frac{z_h}{\delta}}, \text{ Stable} \\ \frac{0.15\delta}{\sigma_u}, \text{ Unstable} \end{cases} \tag{23}$$

$$T_w^L = \begin{cases} 0.5\frac{z_h}{\sigma_w}, \text{ Neutral} \\ \left(\frac{0.1\delta}{\sigma_w}\right)\left(\frac{z_h}{\delta}\right)^{0.8}, \text{ Stable} \\ \frac{0.15\delta}{\sigma_w}\left[1 - \exp\left(\frac{-5z_h}{\delta}\right)\right], \text{ Unstable} \end{cases} \tag{24}$$

While Souaiby and Porté-Agel (2026) used inputs from the LES for the empirical relations, we use Equations 18 - 22 to estimate inputs for the empirical relations of Hanna (1984), yielding a fully self-contained approach. The only inputs required

https://doi.org/10.5194/wes-2026-210
Preprint. Discussion started: 17 November 2026
© Author(s) 2026. CC BY 4.0 License.



eawe european academy of wind energy
Open Access WIND ENERGY SCIENCE DISCUSSIONS

to estimate the spanwise and vertical turbulence intensity and Lagrangian integral timescales using the approach described above are u_*, U_h, z_h, and ϕ. It is to be noted, however, that for the JHTDB dataset, the friction velocity was not available. As a result, the streamwise turbulence intensity and boundary layer height in these cases were prescribed from the precursor simulations, whereas the spanwise and vertical turbulence intensity and integral timescales were estimated using the empirical relations given above. The model results using the empirical framework for input parameters will be referred to as 'Model-v2' in the rest of the article. For practical applications, one could obtain the inputs for the model from turbine manufacturer data (for thrust coefficient and hub height), and from a reanalysis dataset for inputs related to site conditions (such as friction velocity, hub height velocity, and stability conditions).

3.5 Abkar reference model

In addition to the analytical framework described in the previous sections, we also tested an existing framework as a reference. The wake model for stand-alone turbine deficit is one of the best-performing ones in the recent model benchmark performed by Dar and Bachynski-Polić (2026). The model is based on several works (Bastankhah and Porté-Agel, 2014; Abkar et al., 2018; Niayifar and Porté-Agel, 2016; Carbajo Fuertes et al., 2018).

The maximum normalized wake velocity deficit is expressed as:

$$C(x) = \begin{cases} 1 - \sqrt{1 - \frac{C_T}{8(\frac{\sigma(x)}{D})^2}}, & x \geq x_{nw} \\ 1 - \sqrt{1 - C_T}, & x < x_{nw} \end{cases}. \tag{25}$$

The near-wake length is estimated using the following equation (Bastankhah and Porté-Agel, 2016):

$$\frac{x_{nw}}{D} = \frac{1 + \sqrt{1 - C_T}}{\sqrt{2}[4\alpha I_{u,in} + 2\beta(1 - \sqrt{1 - C_T})]}, \tag{26}$$

where $\alpha = 0.9$ and $\beta = 0.077$ are model coefficients (Carbajo Fuertes et al., 2018), and $I_{u,in}$ is the inflow streamwise turbulence intensity. The expansion of the wake is assumed to be linear, and therefore, the wake width can be expressed as:

$$\frac{\sigma}{D} = k_w \frac{x - x_{nw}}{D} + \frac{\sigma_0}{D}, \tag{27}$$

where k_w is the wake growth rate, and σ_0 is the wake width at the start of the far-wake. Bastankhah and Porté-Agel (2016) theoretically estimated σ_0/D to be equal to $1/\sqrt{8}$. Several empirical relations have been proposed to relate the wake growth rate with the streamwise turbulence intensity (Niayifar and Porté-Agel, 2016; Trabucchi et al., 2017; Carbajo Fuertes et al., 2018; Brugger et al., 2019). Here, we choose the relation proposed by Niayifar and Porté-Agel (2016), as this showed the best performance in the comparative study (Dar and Bachynski-Polić, 2026). According to this relation, the wake growth rate can

https://doi.org/10.5194/wes-2026-210
Preprint. Discussion started: 17 November 2026
© Author(s) 2026. CC BY 4.0 License.



be estimated as:

$$k_w = 0.3837 I_{u,in} + 0.0037. \tag{28}$$

The wake shape can be expressed using the skewed Gaussian (Abkar et al., 2018):

$$f(x,y,z,\sigma(x)) = \exp\left(-\frac{1}{2(\sigma(x)/D)^2}\left[\left(\frac{y+\Delta y(x,z)}{D}\right)^2 + \left(\frac{z-z_h}{D}\right)^2\right]\right), \tag{29}$$

where

$$\Delta y(x,z) = x\ \tan(\alpha_v). \tag{30}$$

For waked turbines, the added streamwise turbulence intensity is estimated using the Crespo model (Crespo and Hernández, 1996):

$$I_a^u = 0.73 a_T^{0.8325} I_{u,in}^{-0.0325} (x/D)^{-0.32}. \tag{31}$$

The total streamwise turbulence intensity for the waked turbine is estimated using the local cumulative superposition approach for turbulence intensity described in Section 3.3. The updated turbulence intensity is used to compute the wake growth rate and near-wake length for the waked turbines. Finally, the local superposition principle described in Section 3.3 is used to compute the total wake velocity deficit.

4 Results

Detailed comparisons between the LES, the developed analytical framework, and the reference analytical model are made in this section. Key model outputs are compared, and a quantification of the error in analytical model predictions is made.

4.1 Single turbine cases

Prediction capabilities of the analytical models against the LES data for a single turbine wake are first assessed. We compare the maximum normalized streamwise wake velocity deficit between the analytical models and the LES in Figure 7. The proposed analytical framework with the input data from the LES precursor (Model-v1) can predict the maximum wake deficit in the far wake with good accuracy across all cases. In addition, the analytical framework with empirical inputs (Model-v2) yields comparable results to Model-v1 in most cases, except for the SOWFA-U3 case, in which case an over-prediction of $C(x)$ is observed. The reference Abkar model shows reasonable performance for some cases with neutral and unstable conditions (such as SOWFA-N2,U2,U3 cases), however, it tends to over-predict $C(x)$ in the far wake in stable conditions due to low turbulence

https://doi.org/10.5194/wes-2026-210
Preprint. Discussion started: 17 November 2026
© Author(s) 2026. CC BY 4.0 License.



eawe european academy of wind energy
Open Access WIND ENERGY SCIENCE DISCUSSIONS

levels, and under-predict in SOWFA-N3 case. Overall, it can be concluded that if the inflow boundary layer characteristics are known, the developed analytical framework can provide accurate estimation of $C(x)$ for a single turbine wake in a wide range of stability, veer and turbulence conditions. In case direct inflow measurements are unavailable, the empirical relations used to estimate inflow inputs for the model can yield good results as well, with limited drop in accuracy observed in some cases. Finally, the reference model shows inconsistent performance, with good predictions in moderate turbulence and stability conditions. In the near wake, all models use the one-dimensional momentum theory to estimate $C(x)$, which leads to an under-prediction in its magnitude in the stable and neutral cases compared to LES, as the effect of pressure gradient in the near wake is unaccounted for in the analytical models. This, however, is not a concern, as the study is focused primarily on the far-wake modelling of the wake velocity deficit. The results presented here use the modified spreading rate for stable cases due to the presence of an LLJ in the inflow. The effect of this modification is further discussed in A.

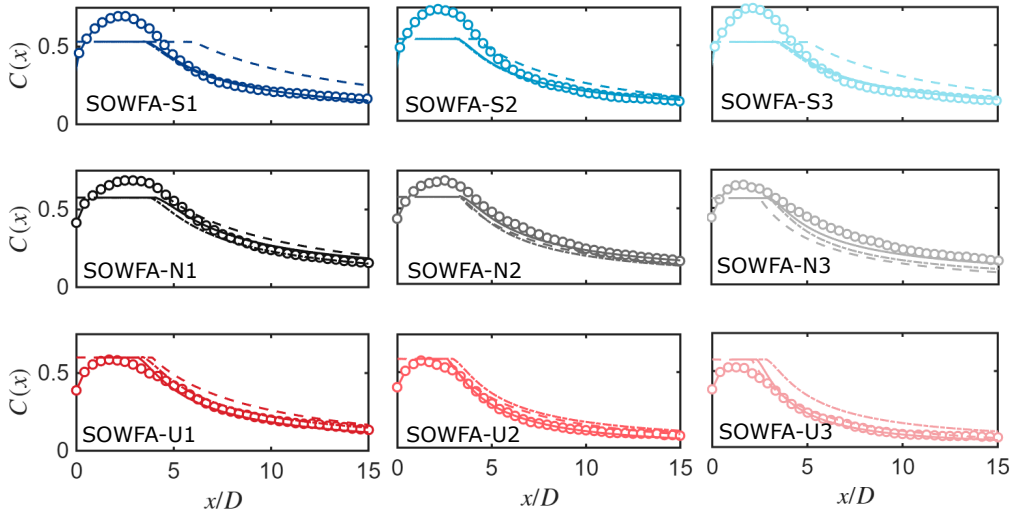


Figure 7. Comparison of the maximum normalized averaged streamwise wake velocity deficit between LES and different models for single turbine cases. Lines with circle markers denote SOWFA results, solid lines show results from Model-v1, dashed-dotted lines represent Model-v2, and dashed lines are predictions from the Abkar model.

https://doi.org/10.5194/wes-2026-210
Preprint. Discussion started: 17 November 2026
© Author(s) 2026. CC BY 4.0 License.



eawe european academy of wind energy
Open Access WIND ENERGY SCIENCE DISCUSSIONS

The cross-stream contours of the normalized averaged wake velocity deficit are also compared between the LES and the analytical models at selected streamwise locations in Figure 8. The Model-v2 results (not shown) are very close to those of Model-v1. Both the proposed analytical framework and the Abkar model can predict the skewed wake shape due to veer effect in stable and neutral cases. The proposed framework shows a slightly smaller skewness compared to the Abkar model, which is particularly noticeable in the far wake of the stable cases, and shows a relatively better comparison with the LES data. This is due to the modified skewness correction term, which accounts for the change in the veer in the wake compared to that in the inflow. In some unstable cases (SOWFA-U2,U3), a wake offset in the spanwise direction is also observed due to a non-zero hub height wind direction, which is also captured by both models. In terms of the wake deficit magnitude and shape, the proposed framework shows a better comparison with the LES data relative to the Abkar model due to better predictions of $C(x)$ and $\sigma(x)$.

Finally, we attempt to quantify the errors in the predictions of the normalized averaged wake velocity deficit from different analytical models relative to the LES data. For this purpose, we compute the root-mean-square error (RMSE) in the cross-stream planes at each streamwise location in the wake. The RMSE is computed over the wake region where the normalized averaged deficit is greater than 2% in the LES data. This approach defines a wake boundary from the LES and then computes the RMSE of the models over this bounded wake region. Figure 9 shows the RMSE of all models for all cases. The proposed analytical model with measured inflow inputs (Model-v1) shows the lowest RMSE for each respective case among all the models. In the far-wake at $x/D > 7$, the RMSE is consistently below 5% for all cases, with the unstable cases showing the lowest RMSE. The proposed model with empirical inputs Model-v2 shows comparable RMSE to Model-v1, except for the SOWFA-U2,U3 cases. In the latter cases, the RMSE is still below 5% for Model-v2, showing good accuracy. This indicates that in the absence of measured input data, the empirical inputs can be used without a significant loss of model accuracy. The Abkar model shows comparable RMSE to Model-v1 for the unstable cases, however, for neutral and stable cases, the RMSE is higher, with values exceeding 1.5 times those of the Model-v1 in highly stable cases. Since Model-v2 is observed to yield similar results to Model-v1, in the following sections, we will only discuss any exceptions to this observation for the sake of brevity.

4.2 Turbine array cases

Analytical model predictions for the three turbine array are now compared with the LES results. Figure 10 shows the maximum normalized averaged streamwise wake velocity deficit obtained from the LES and the analytical models. The proposed analytical framework in its two versions demonstrates good agreement with the LES data, which validates the use of the waked turbine considerations introduced in Section 3.2. The sensitivity of the model results to the turbine-modified integral timescales is further discussed in B. The Abkar model, on the other hand, tends to under-predict $C(x)$, which is particularly noticeable in the cumulative wake of the three turbines. This can be related to an under-prediction of the near-wake length, as the model appears to start recovery of the maximum wake deficit at an earlier position compared to the LES and the proposed models in the cumulative wake of the turbine array.

https://doi.org/10.5194/wes-2026-210
Preprint. Discussion started: 17 November 2026
© Author(s) 2026. CC BY 4.0 License.

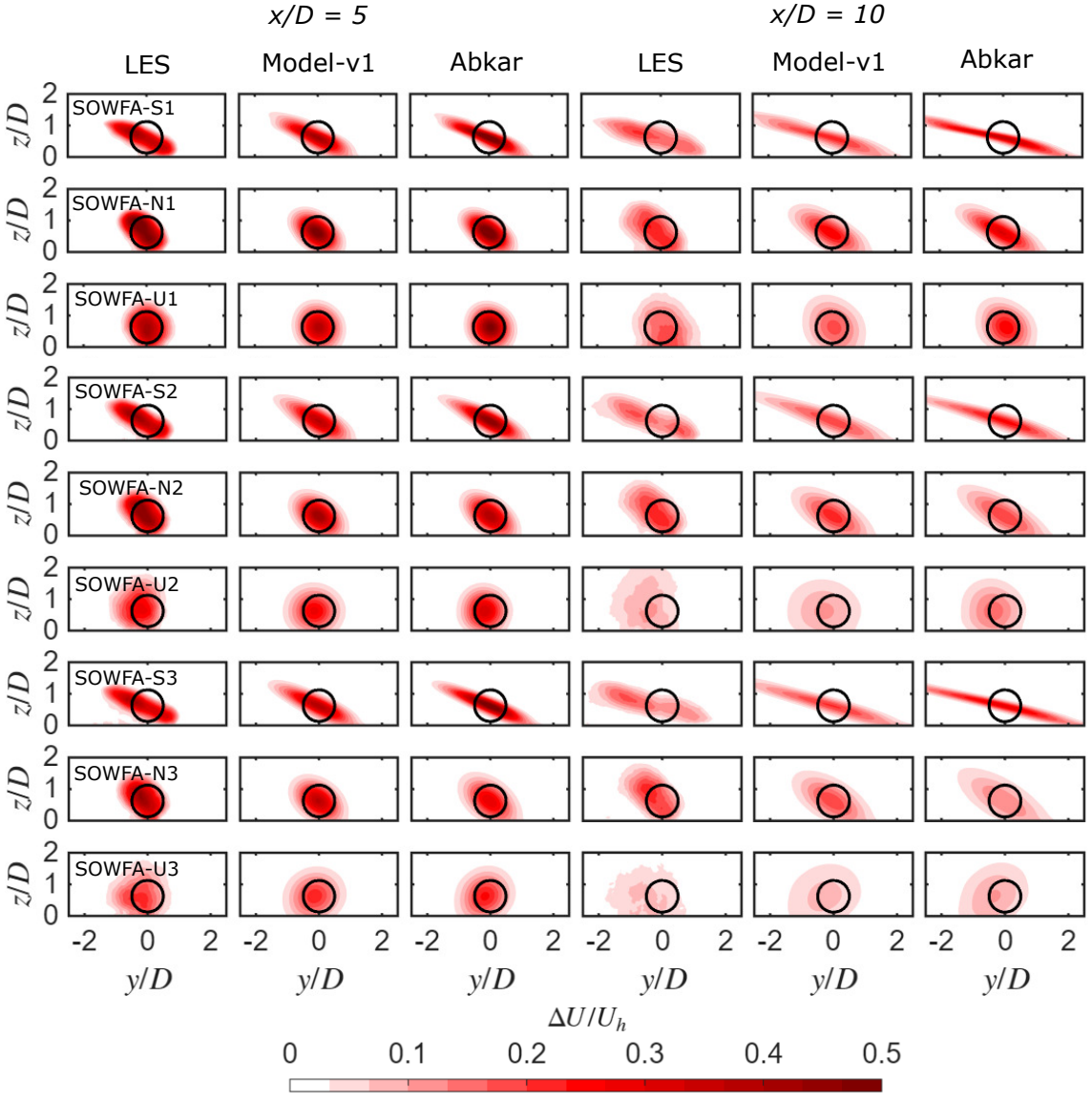


Figure 8. Cross-stream contours of the normalized averaged wake velocity deficit obtained from SOWFA-LES and different analytical models at selected streamwise locations for all single turbine cases. The black circles denote the rotor outline.

Figure 11 shows the contours of the cross-stream normalized averaged streamwise wake velocity deficit at streamwise locations 5 rotor diameters downstream of the second and third turbines. For the unstable cases, both models predict the wake shape well, where the magnitude is well-predicted by the proposed model and under-predicted by the Abkar model in the cumulative wake of the three turbines. For the neutral and stable cases, the Abkar model predicts a higher skew compared to the proposed model. The superposition of the individual turbine wakes can also be identified in the model results via the two differently skewed regions in the cumulative wake, as the wake of the upstream-most turbine has a larger skew compared to

https://doi.org/10.5194/wes-2026-210
Preprint. Discussion started: 17 November 2026
© Author(s) 2026. CC BY 4.0 License.

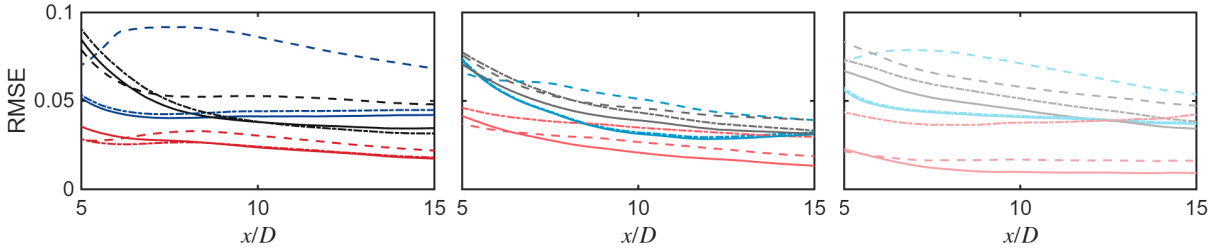


Figure 9. Root-mean-square error (RMSE) between the SOWFA-LES and the analytical models. Solid lines show RMSE of Model-v1, dashed-dotted lines represent Model-v2, and dashed lines are RMSE of the Abkar model. Colors represent different cases as in Figure 3.

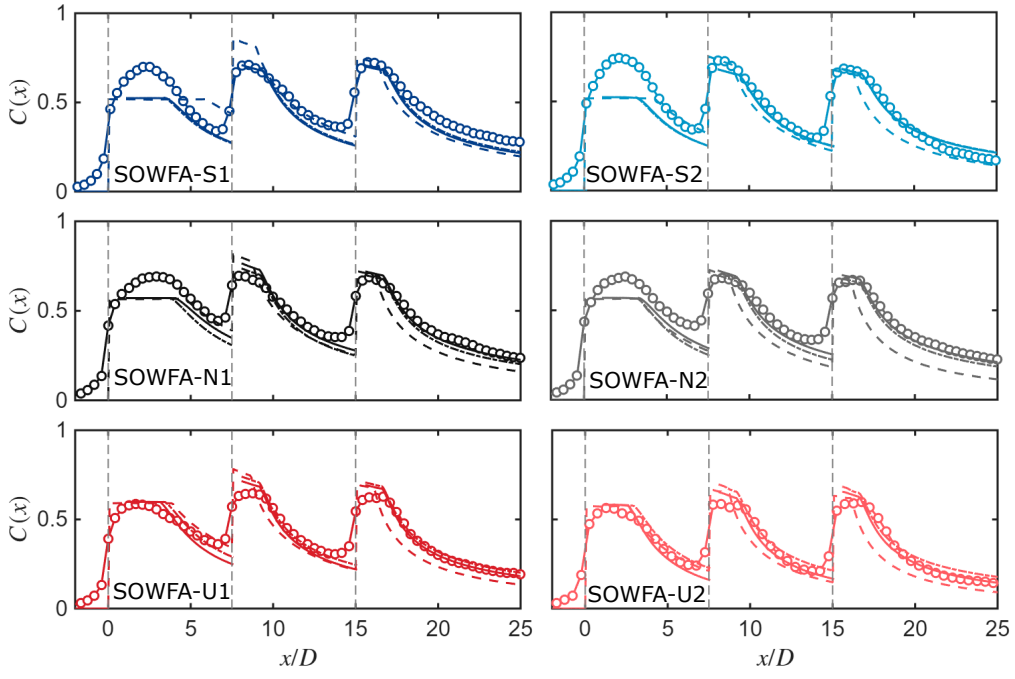


Figure 10. Comparison of maximum normalized averaged wake velocity deficit between LES and different models for array wake cases. Lines with circle markers denote SOWFA results, solid lines show results from Model-v1, dashed-dotted lines represent Model-v2, and dashed lines are predictions from the Abkar model. The vertical dashed gray lines show turbine locations.

the downstream-most turbine. It can also be observed that both models tend to predict a slightly larger skew compared to the LES in the cumulative wake of the three turbines ($x/D = 20$) for the stable cases. This can be related to the fact that both models assume that the wake skewness keeps growing with the increase in the streamwise distance. This assumption may not hold very well for very long distances, which can explain the relatively larger skew in the cumulative wake from the models compared to the LES. Future research should address this in detail.

The RMSE of model predictions is shown in Figure 12 for all models. The RMSE is observed to be higher in the near-wake of the turbines, as well as upstream of the waked turbines for all models. The near-wake RMSE can be explained by the fact that models assume a top-hat wake shape and rely on the one-dimensional momentum theory in this region. As a result, they do

https://doi.org/10.5194/wes-2026-210
Preprint. Discussion started: 17 November 2026
© Author(s) 2026. CC BY 4.0 License.

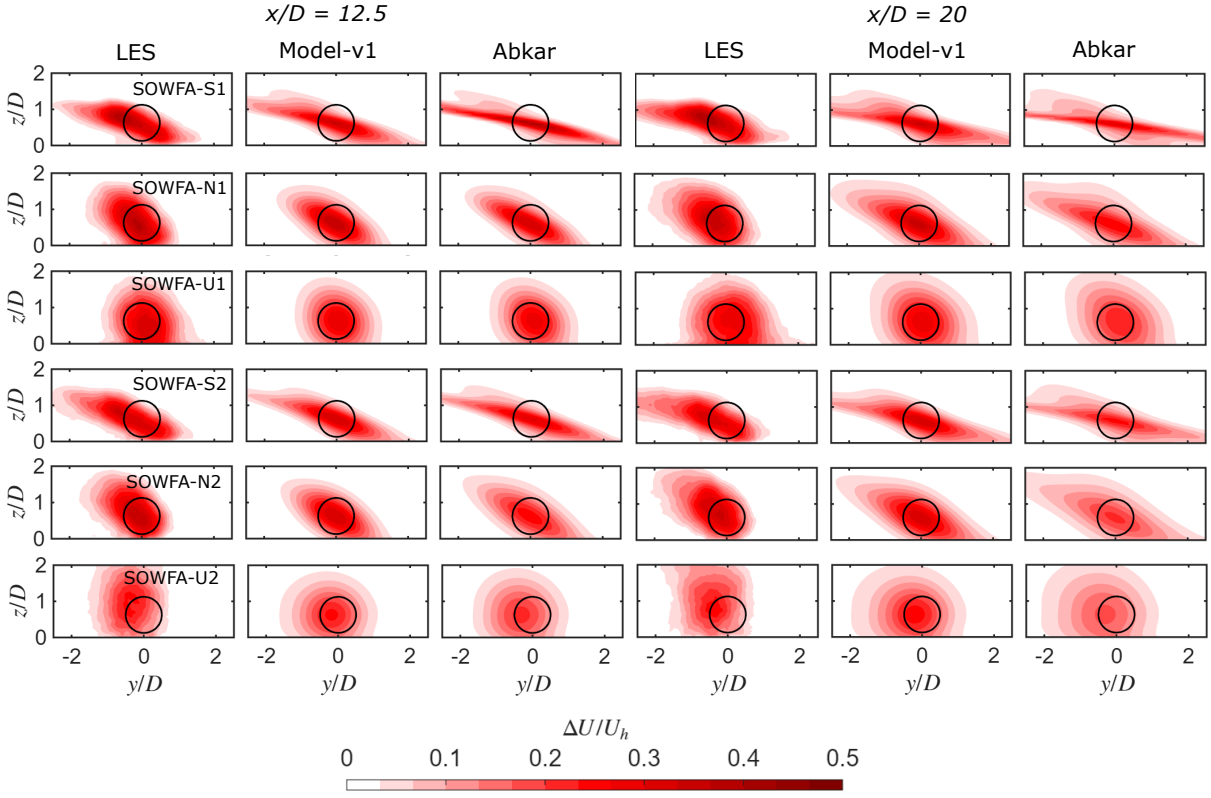


Figure 11. Cross-stream contours of the normalized averaged cumulative array wake velocity deficit obtained from SOWFA-LES and different analytical models at selected streamwise locations downstream the second and third turbines in the array. The black circles denote the rotor outline.

not account for the turbine nacelle effects or the near-wake pressure gradient, which leads to a higher RMSE in this region. The increase in the RMSE in the region upstream of the waked turbines is attributed to the induction region of the turbines, which is not modelled by the analytical models. In the far wake, the RMSE is less than 8% for all cases by the proposed analytical framework(s). The stable cases show the highest RMSE, and the unstable ones show the lowest. This can be (in part) related to the wake skew over-estimation, as discussed earlier. In the cumulative array wake, the RMSE of the Abkar model is higher than the proposed models, except for the SOWFA-U2 case. This shows that the proposed models improve the cumulative wake deficit prediction accuracy compared to the reference Abkar model across all array cases.

4.3 Semi-infinite wind farm in CNBL

The analytical models are now used to predict the wake velocity deficit for the semi-infinite wind farm in a conventionally neutral boundary layer. Figure 13 shows the comparison of the maximum normalized averaged streamwise wake velocity deficit in the wind farm obtained from the LES and the analytical models. The proposed models show excellent agreement with the LES over the entire length of the wind farm. The Abkar model tends to predict a faster recovery of $C(x)$ compared to

https://doi.org/10.5194/wes-2026-210
Preprint. Discussion started: 17 November 2026
© Author(s) 2026. CC BY 4.0 License.

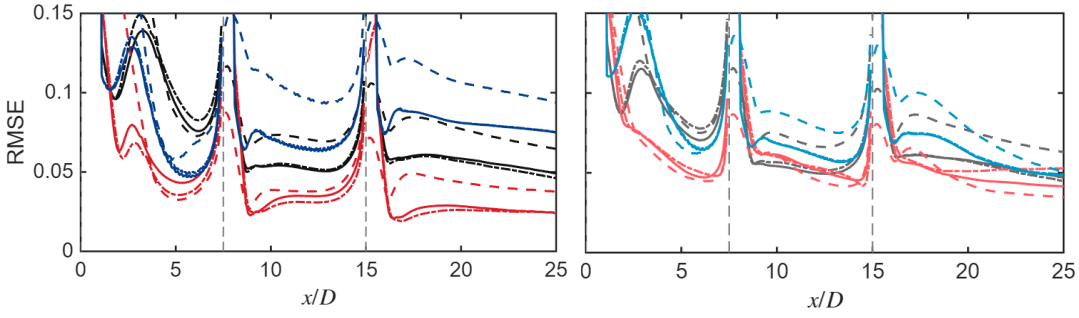


Figure 12. Root-mean-square error (RMSE) between the SOWFA-LES and the analytical models for array wake cases. Solid lines show RMSE of Model-v1, dashed-dotted lines represent Model-v2, and dashed lines are RMSE of the Abkar model. Colors represent different cases as in Figure 3.

the LES and the proposed models. This is consistent with the observations of Souaiby and Porté-Agel (2024), which showed that standard analytical models tend to predict a faster wake recovery for large wind farms. They related this to the assumption of the linear wake expansion, which does not hold over very long distances. In addition to the faster expansion due to linear growth, the accumulation of wake-added turbulence intensity over the wind farm results in a faster wake recovery than the LES results in this model. The use of physics-based wake expansion and near-wake length models together with the introduced added turbulence models lead to improved predictions compared to the reference model.

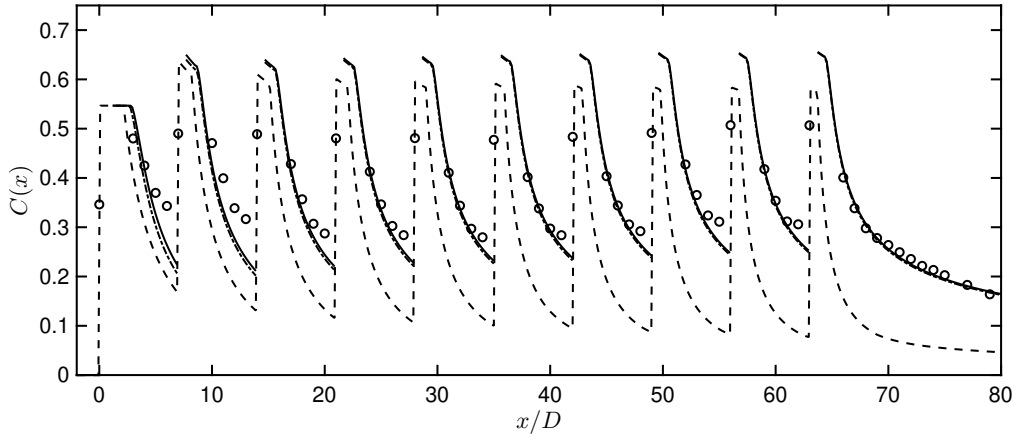


Figure 13. Comparison of maximum normalized averaged wake velocity deficit between LES and different models for the wind farm in CNBL. Circles denote LES data from JHTDB, solid lines show results from Model-v1, dashed-dotted lines represent Model-v2, and dashed lines are predictions from the Abkar model.

We also compare the cross-stream contours of the normalized averaged streamwise wake velocity deficit within and in the wake of the wind farm in Figure 14. The velocity deficit distribution from the proposed model compares significantly better with the LES data relative to the Abkar model. The slight spanwise heterogeneity in the wake shape observed for different turbines in the LES data cannot be captured by the analytical models, as they treat each turbine individually and do not account for

https://doi.org/10.5194/wes-2026-210
Preprint. Discussion started: 17 November 2026
© Author(s) 2026. CC BY 4.0 License.

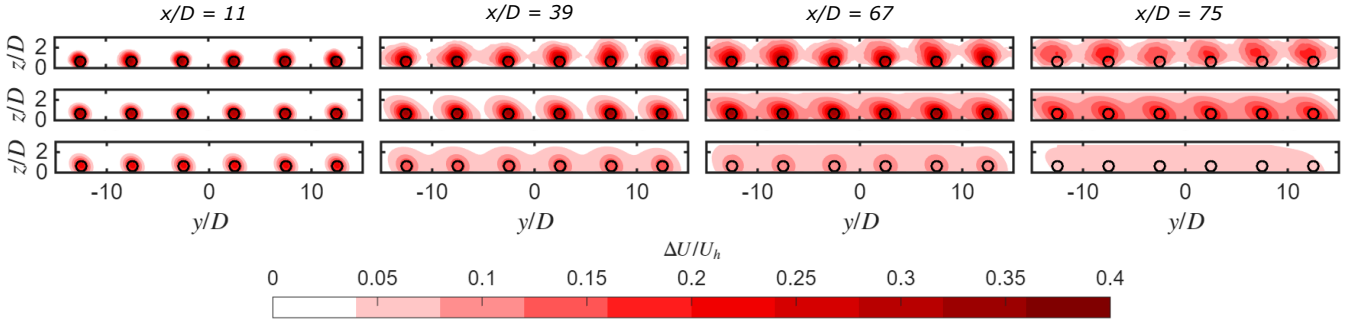


Figure 14. Cross-stream contours of the normalized averaged cumulative wind farm wake velocity deficit obtained from JHTDB-LES and different analytical models at selected streamwise locations within and downstream of the wind farm. The top, middle and bottom rows show LES, Model-v1 and Abkar model results, respectively. Black circles represent rotor periphery.

The RMSE in the prediction of the wake velocity deficit from different analytical models is compared in Figure 15. For the two proposed model versions, there are slight differences in the first two rows, beyond which they have similar errors. The RMSE is approximately constant over the wind farm, with values lying below 5% for the most part. The Abkar model has a slightly higher RMSE in the first rows of the farm ($\approx 6\%$), however, from the fourth row onwards, the RMSE steadily grows to around 10%. In the farm wake, the RMSE starts to go down, which can be related to the eventual recovery of the farm wake in the LES.

4.4 Semi-infinite wind farm in a diurnal cycle

Thermal stability, atmospheric turbulence, and wind veer vary over a diurnal cycle due to changes in the heating of the Earth's surface and its effect on the atmospheric boundary layer. Daytime boundary layers are, generally, characterized by unstable, highly turbulent, and relatively large boundary layer heights, whereas nighttime boundary layers are stable, with low turbulence, and low height. Transitional boundary layers between night and day also exist, which show more complicated characteristics than purely unstable or stable boundary layers.

In this section, we assess the performance of the analytical models against LES data from JHTDB across a diurnal cycle. Figure 16 shows a comparison of the maximum normalized averaged streamwise wake velocity deficit at different times of the day between the analytical models and the LES results. The proposed model in its two versions shows good agreement with the LES data for all selected times of the day, except the late afternoon. As discussed in Section 2.3, at noon and early afternoon,

https://doi.org/10.5194/wes-2026-210
Preprint. Discussion started: 17 November 2026
© Author(s) 2026. CC BY 4.0 License.



eawe european academy of wind energy
Open Access WIND ENERGY SCIENCE DISCUSSIONS

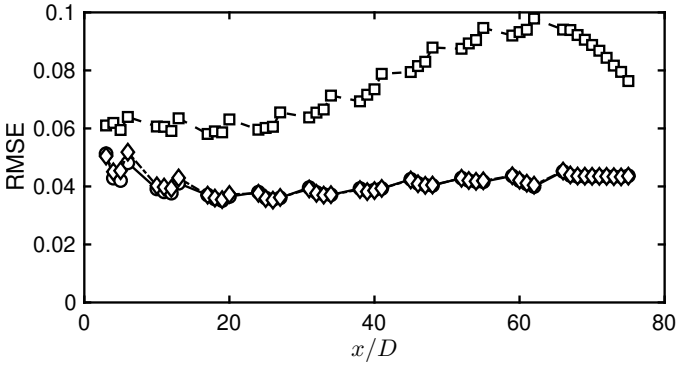


Figure 15. Root-mean-square error (RMSE) between the JHTDB-LES and the analytical models for the wind farm in CNBL. Solid lines with circle markers show RMSE of Model-v1, dashed-dotted lines with diamond markers represent Model-v2, and dashed lines with square markers are RMSE of the Abkar model.

the boundary layer is unstable, whereas at evening and early morning, it is stable, with a transitional boundary layer in the late afternoon. While the model works well in purely unstable or stable boundary layers, it may not capture complex wake characteristics in a transitional boundary layer, which may explain its inability to capture the maximum wake deficit recovery trend. It is to be noted that, as the wind farm experienced an LLJ in the early morning, the model used the modified spreading rate for this time, validating its effectiveness beyond the SOWFA simulations. For the evening time, the original spreading rate is used, which confirms that for stable boundary layers without a low-level jet, no modification to the spreading rate is needed. The Abkar model tends to predict a faster rate of recovery for noon, early and late afternoon times, where the under-prediction of the deficit increases behind each row. Once again, this can be related to the under-prediction of the near-wake length and over-prediction of the wake expansion in the farm. For the evening and early morning times, the prediction of the Abkar model is relatively better, with slight under-prediction in the wake of the whole wind farm in the evening case, and an over-prediction in the second row in the early morning scenario. Figure 17 shows the normalized cross-stream contours of the averaged streamwise wake velocity deficit at 4 rotor diameters behind the turbines in each row, obtained from the LES and the analytical models. Overall, the proposed modelling framework performs better than the reference one in reproducing the wake shape and deficit magnitude for all times. For the noon and afternoon times, a deflection of the wake in the spanwise direction is seen in the LES data. This is due to the fact that the turbines are not aligned with the incoming wind direction, and a non-zero wind direction across the rotor leads to a spanwise offset in the wake centre position. This also implies that the downstream turbines do not experience full wake conditions, rather they are in the partial wake of the upstream turbines. The spanwise wake offset is well captured by both analytical models through the veer correction term, where the wake shape and magnitude are better reproduced by the proposed model. The two turbine wakes at a given streamwise position show some differences in magnitude in the LES, especially in the noon and afternoon times. Similar to the CNBL case, this may be contributed by the inter-turbine effects in a spanwise infinite wind farm. In addition, the unstable boundary layers can have larger spanwise variations in the averaged velocity profile due to high- or low-speed zones created by large convective structures in the flow (Cheung et al., 2024). Since the velocity deficit for these cases is computed using a spanwise-averaged velocity profile upstream of the wind

https://doi.org/10.5194/wes-2026-210
Preprint. Discussion started: 17 November 2026
© Author(s) 2026. CC BY 4.0 License.

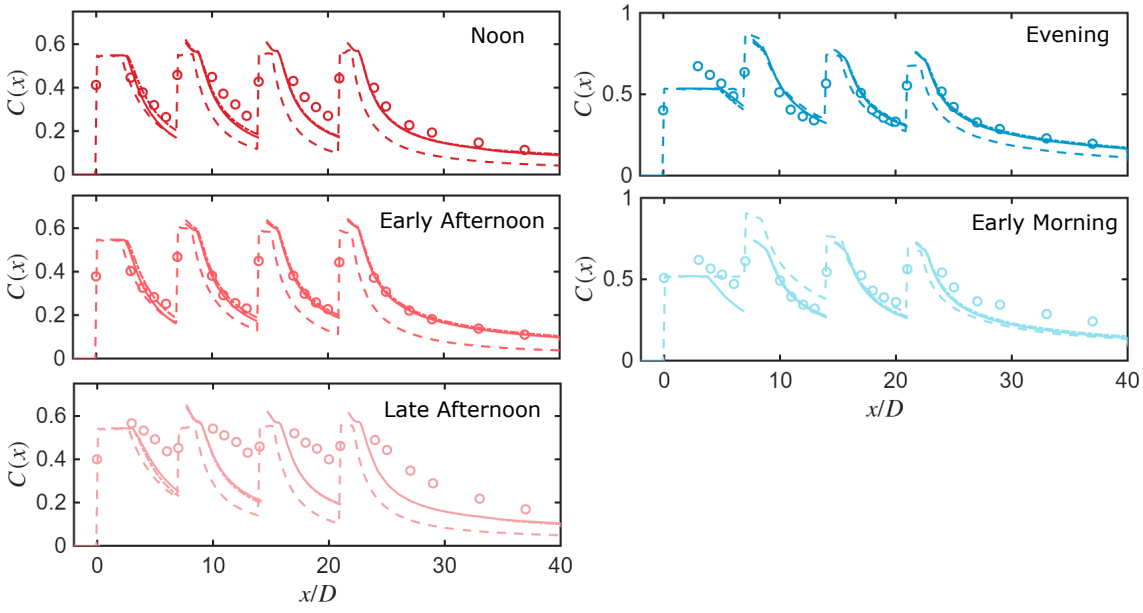


Figure 16. Comparison of maximum normalized averaged wake velocity deficit between JHTDB-LES and different models in the diurnal cycle. Circles denote LES data, solid lines show results from Model-v1, dashed-dotted lines represent Model-v2, and dashed lines are predictions from the Abkar model.

farm, some of these local variations in the velocity are unaccounted for, and may also have a contribution to the differences in the wake shape and magnitude of the two turbines at a given streamwise position. The analytical models, on the other hand, yield similar wakes for the two turbines at a given streamwise position, as they do not account for spanwise inter-turbine effects in a semi-infinite farm, and the undisturbed flow is assumed to be homogeneous in the horizontal directions.

For the evening scenario, the proposed model reproduces the wake deficit quite well behind the first and second turbine row, however, behind the third and fourth row, the LES shows a wider wake deficit region than the analytical models. As discussed in Section 4.2, this can be related to the fact that both models (although with different magnitudes) assume that the wake skewness keeps increasing with the increase in the streamwise distance. This results in a more laterally stretched wake for long distances, such as in the farm wake. This is an area that needs further exploration in future research. In the early morning, the wind farm blockage significantly affects the velocity deficit within the wind farm in these simulations, as also discussed by Xiao et al. (2025). This is evident from the non-zero velocity deficit throughout the span of the wind farm behind the first row of turbines (see e.g., $x/D = 4$ at early morning in Figure 17). This effect weakens as we go further downstream within and behind the farm, however, it appears to persist throughout the farm wake. As the analytical models do not account for the blockage effects, they cannot reproduce the observed velocity deficit throughout the span of the farm, but do predict the wake velocity deficit, with similar observations as for the evening scenario.

Finally, we compare the RMSE of the analytical models in Figure 18. For noon and early afternoon, the proposed models show approximately constant RMSE over the entire length of the farm, which is below 6%. For the late afternoon, the RMSE

https://doi.org/10.5194/wes-2026-210
Preprint. Discussion started: 17 November 2026
© Author(s) 2026. CC BY 4.0 License.

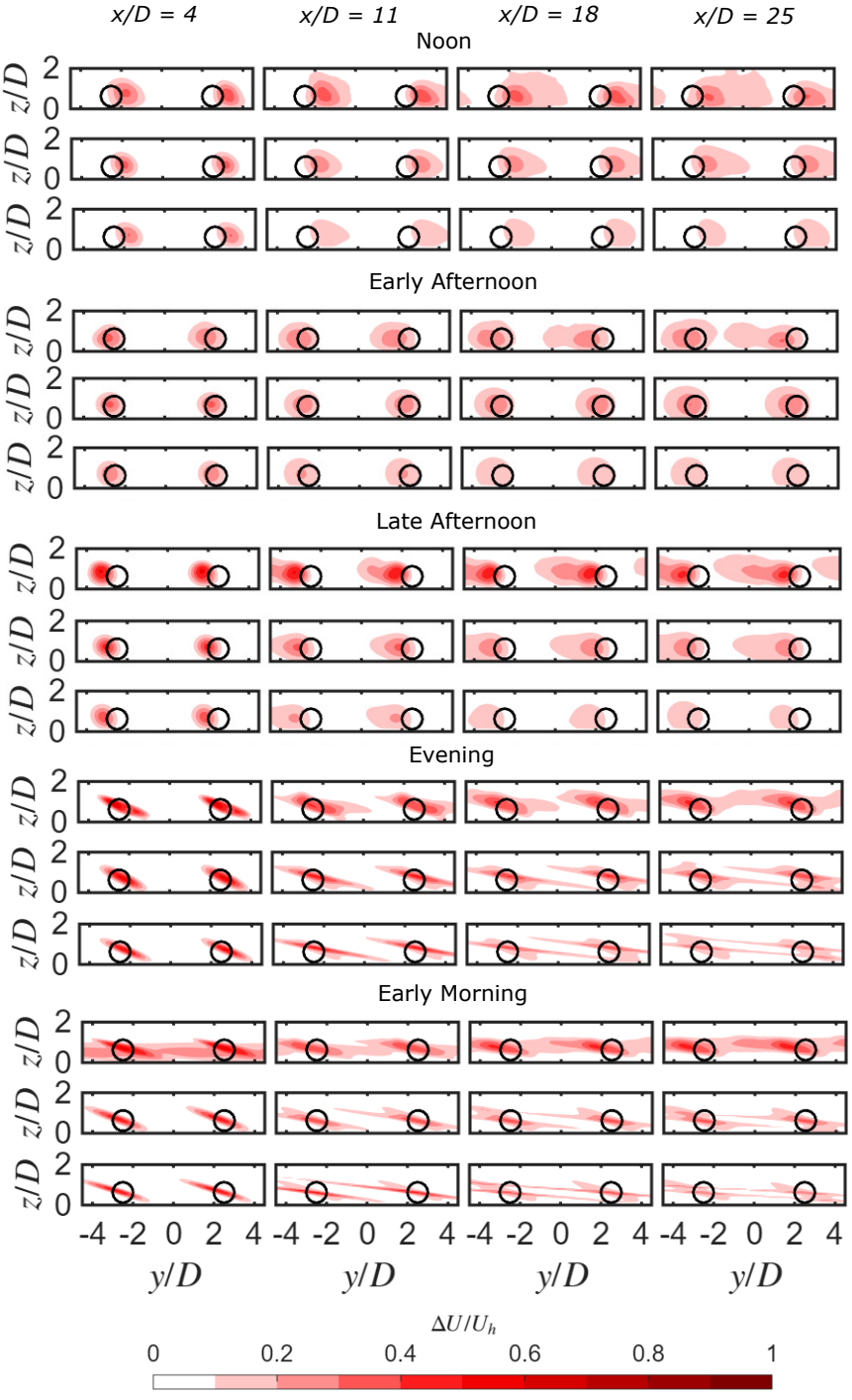
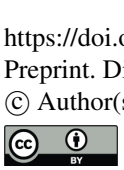


Figure 17. Cross-stream contours of the normalized averaged cumulative wind farm wake velocity deficit obtained from JHTDB-LES and different analytical models at selected streamwise locations within and downstream of the wind farm in a diurnal cycle. For each time of day, the top, middle, and bottom rows show LES, Model-v1, and Abkar model results, respectively. Black circles represent the rotor periphery.

https://doi.org/10.5194/wes-2026-210
Preprint. Discussion started: 17 November 2026
© Author(s) 2026. CC BY 4.0 License.



eawe european academy of wind energy
Open Access WIND ENERGY SCIENCE DISCUSSIONS

is around 8% behind the first two turbine rows, but shows a reduction from the third row onwards. For the evening case, the RMSE of the proposed models is initially around 7% behind the first row, but grows to about 8-9% over the length of the wind farm. The higher skewness in the wake of the analytical models compared to the LES at large downstream distances explains the increase in the RMSE over the length of the wind farm. For the early morning scenario, the RMSE is highest compared to the rest of the tested situations. This is attributed to the wind farm blockage in this scenario, which is not captured by the analytical models. The RMSE is initially around 18% behind the first row, but decreases to slightly below 10% behind the second row. This is consistent with the fact that the blockage effect is highest in the entrance region and the first row of turbines. Behind the third and fourth turbine rows, the RMSE increases compared to that behind the second turbine row. This can be related to the higher predicted skewness of the wake by the analytical models compared to the LES. The Abkar model consistently shows higher RMSE compared to the proposed models, which indicates that the proposed analytical framework can improve the prediction accuracy over the reference model throughout the diurnal cycle.

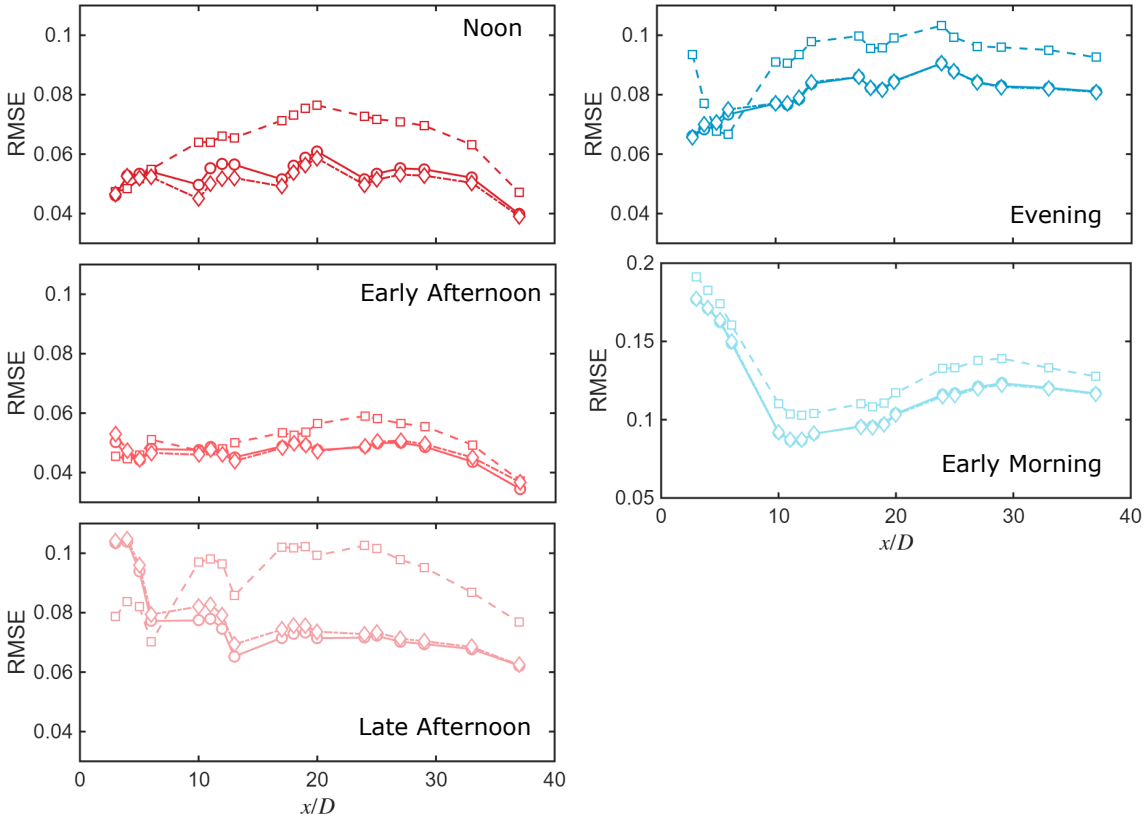


Figure 18. Root-mean-square error (RMSE) between the JHTDB-LES and the analytical models for the wind farm in a diurnal cycle. Solid lines with circle markers show RMSE of Model-v1, dashed-dotted lines with diamond markers represent Model-v2, and dashed lines with square markers are RMSE of the Abkar model.

https://doi.org/10.5194/wes-2026-210
Preprint. Discussion started: 17 November 2026
© Author(s) 2026. CC BY 4.0 License.



eawe european academy of wind energy
Open Access WIND ENERGY SCIENCE DISCUSSIONS

5 Summary and concluding remarks

Analytical models offer a fast and accurate approach to model wind farm wake velocity deficit, making them ideal for practical applications. While a large body of literature on analytical models already exists, there is an obvious research gap in the development of an analytical modelling framework that can predict the wake velocity deficit of a wind farm under different thermal stability, wind veer, and turbulence conditions.

In this work, we addressed this gap by proposing a novel analytical framework that utilizes a physics-based model for wake expansion together with a veer-aware wake velocity deficit model to predict the wake velocity deficit of a wind turbine in a range of atmospheric boundary layer conditions. We addressed relevant considerations regarding the treatment of waked turbines, and introduced new relations for turbine-modified cross-stream integral timescales and wake-added cross-stream turbulence intensities. For scenarios where direct measurements of key atmospheric boundary layer characteristics are unavailable, a separate framework to obtain these inputs using empirical relations available in the literature was also proposed.

In order to aid the development and subsequent testing of the modelling framework, we performed large-eddy simulations of a single turbine wake exposed to nine different boundary layers varying in thermal stability, wind veer, atmospheric turbulence, and occurrence of low-level jets. The single turbine data were used to assess the integration of the physics-based wake expansion model with the veer-aware velocity deficit model, and to develop relations for turbine-modified integral timescales and cross-stream turbulence intensity models. A three turbine array under six different atmospheric conditions was then simulated to test the performance of the modelling framework. In addition to the simulations performed in this study, LES data from the Johns Hopkins University turbulence database of wind farms under a neutral boundary layer, and at selected times over a diurnal cycle, were also used to assess and validate the proposed analytical framework.

The proposed analytical framework was tested in two different versions: first, where the inputs for the model were obtained from precursor LES simulations; and second, using the proposed framework to obtain these inputs based on site and flow conditions. Results from a reference analytical framework were also included as a benchmark for comparison. The proposed framework with inputs from the precursor data showed the closest agreement to the LES data among all analytical models, and showed a clear improvement in prediction accuracy over the reference modelling framework for all tested scenarios ranging from single turbine wake to semi-infinite wind farms. The utilization of the empirical framework to obtain input parameters had a very limited effect on the model results.

In order to quantify the prediction accuracy, the root-mean-square error of analytical model predictions was computed. The proposed analytical framework in its two versions showed lower RMSE compared to the reference modelling framework, with values typically below 5% in the single wake cases, below 8% in the array wake cases, and below 5% for the semi-infinite wind farm in neutral conditions in the far wake. For the semi-infinite wind farm in a diurnal cycle, the performance varied with the time of the day, and complexity of the atmospheric flow. The reference model showed RMSE higher than the proposed model for all selected times. In general, the model showed the lowest RMSE in unstable conditions and the highest in stable ones. The relatively higher RMSE in the farm wakes under stable conditions was related to the assumption of the scaling of the wake skewness with streamwise distance, which may not hold over very long distances. In addition, in the early morning,

https://doi.org/10.5194/wes-2026-210
Preprint. Discussion started: 17 November 2026
© Author(s) 2026. CC BY 4.0 License.



eawe european academy of wind energy
Open Access WIND ENERGY SCIENCE DISCUSSIONS

farm blockage had a significant effect on wake deficit within the wind farm, resulting in the highest RMSE over all test cases. Both these effects need to be studied and addressed in detail in future research.

Overall, we have demonstrated the capability of the proposed analytical framework to predict wind farm wake velocity deficit in diverse atmospheric conditions varying in the thermal stability class and magnitude, wind veer magnitude, turbulence levels, and occurrence and location of low-level jets under stable conditions. The analytical framework can prove useful to account for wake effects under such conditions for layout optimization, annual energy production calculations, wake control or other applications requiring fast and accurate wake estimates.

Appendix A: Sensitivity to the spreading rate for cases with LLJ

Figure A1 shows the effect of spreading rate on the model predictions for the stable cases with an LLJ. Using the original spreading rate of the mixing layer for these cases results in a slower recovery of $C(x)$. As the spreading rate is increased, the model predicts a faster recovery in agreement with the LES data. As discussed in previous studies (Doosttalab et al., 2020; Gadde and Stevens, 2021), an LLJ around the rotor top tip enhances wake meandering and makes the mixing layer unstable. This is consistent with an effective increase in the spreading rate parameter, as implemented in this study. Therefore, our modification of the spreading rate is in line with the underlying physical mechanisms governing the recovery of the wake.

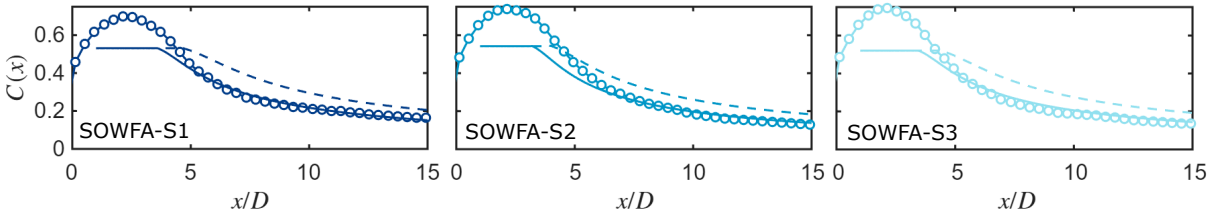


Figure A1. Comparison of maximum normalized averaged wake velocity deficit between LES and the analytical model for different spreading rates in stable cases with an LLJ. Lines with circle markers denote the LES data, solid lines show results with the modified spreading rate $S' = 0.07$, and the dashed lines show results with the original spreading rate $S' = 0.043$.

Appendix B: Sensitivity to the turbine-modified integral timescale

In Section 3.2.2 we noted that the ratio of the Eulerian integral timescales in the wake to the characteristic timescale of the rotor ranged between 0.2 and 0.6 for all cases in the turbine wake(s). For simplicity, we chose the rotor radius and inflow velocity to define the Eulerian integral timescales in the wake flow. In this section, we explore the sensitivity of the model to the choice of turbine-modified integral timescales. Figure B1 shows the maximum normalized streamwise wake velocity deficit for the three turbine array from SOWFA simulations, and the model results based on four different choices for the turbine-modified integral timescales. These choices are: (i) $T_v^E = T_w^E = D/2U_{in}$ (the choice used in the study), (ii) $T_v^E = T_w^E = D/4U_{in}$, (iii) $T_v^E = T_w^E = 3D/4U_{in}$, and (iv) $T_v^E = 3D/4U_{in}$, and $T_w^E = D/4U_{in}$. Reducing the integral timescales tends to increase the rate of wake recovery, whereas increasing the integral timescales has the opposite effect. The effects are non-linear, since

https://doi.org/10.5194/wes-2026-210
Preprint. Discussion started: 17 November 2026
© Author(s) 2026. CC BY 4.0 License.

reducing the timescales from $D/2U_{in}$ to $D/4U_{in}$ has a relatively smaller effect than increasing it to $3D/4U_{in}$. The choice based on the unequal integral timescales for the spanwise and vertical directions, also seems to have no significant influence on the results. Overall, one can conclude that the model results are not extremely sensitive to the particular choice of integral timescales, as long as the choice is based on the characteristic timescale of the rotor defined by the rotor radius and inflow velocity.

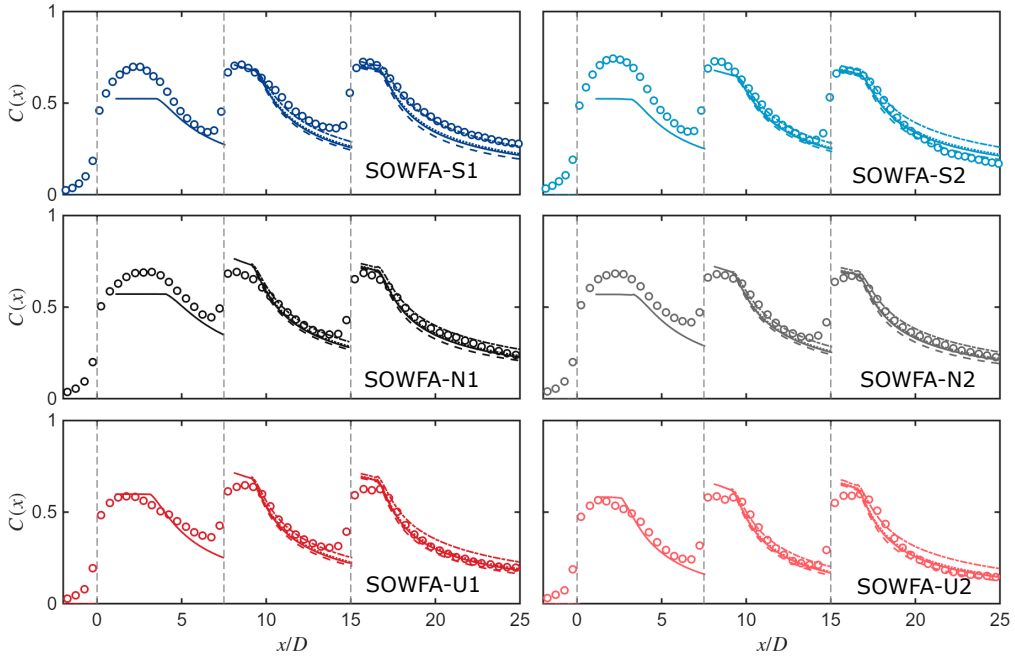


Figure B1. Comparison of maximum normalized averaged wake velocity deficit between LES and the analytical model for different turbine-modified integral timescales. Circles markers denote the LES data, solid lines show model results with $T_v^E = T_w^E = D/2U_{in}$, the dashed-dotted lines show results with $T_v^E = T_w^E = D/4U_{in}$, the dashed lines show results with $T_v^E = T_w^E = 3D/4U_{in}$, and dotted lines show results with $T_v^E = 3D/4U_{in}$, and $T_w^E = D/4U_{in}$.

Author contributions. ASD: Conceptualization, Methodology, Investigation, Formal analysis, Data curation, Writing - Original Draft. EEB-P: Conceptualization, Methodology, Supervision, Funding acquisition, Writing - Review & Editing.

Competing interests. EEB-P is an associate editor of *Wind Energy Science*. The authors have no other competing interests to declare.

Data availability. The simulation data can be made available upon reasonable request from the corresponding author.

https://doi.org/10.5194/wes-2026-210
Preprint. Discussion started: 17 November 2026
© Author(s) 2026. CC BY 4.0 License.



Acknowledgements. This research was funded by the Norwegian Research Council under the BIRDWAKE project (grant no. 353053). Computational resources were provided by SIGMA2 under project no. NN12073K.

https://doi.org/10.5194/wes-2026-210
Preprint. Discussion started: 17 November 2026
© Author(s) 2026. CC BY 4.0 License.

References

Abbas, N. J., Zalkind, D. S., Pao, L., and Wright, A.: A reference open-source controller for fixed and floating offshore wind turbines, Wind Energy Science, 7, 53–73, 2022.

Abkar, M. and Porté-Agel, F.: Influence of atmospheric stability on wind-turbine wakes: A large-eddy simulation study, Physics of fluids, 27, 2015.

Abkar, M. and Porté-Agel, F.: Influence of the Coriolis force on the structure and evolution of wind turbine wakes, Physical Review Fluids, 1, 063 701, 2016.

Abkar, M., Sharifi, A., and Porté-Agel, F.: Wake flow in a wind farm during a diurnal cycle, Journal of Turbulence, 17, 420–441, 2016.

Abkar, M., Sørensen, J. N., and Porté-Agel, F.: An analytical model for the effect of vertical wind veer on wind turbine wakes, Energies, 11, 1838, 2018.

Ali, K., Stallard, T., and Ouro, P.: A diffusion-based wind turbine wake model, Journal of Fluid Mechanics, 1001, A13, 2024.

Antonini, E. G. and Caldeira, K.: Atmospheric pressure gradients and Coriolis forces provide geophysical limits to power density of large wind farms, Applied Energy, 281, 116 048, 2021.

Archer, C. L., Vasel-Be-Hagh, A., Yan, C., Wu, S., Pan, Y., Brodie, J. F., and Maguire, A. E.: Review and evaluation of wake loss models for wind energy applications, Applied Energy, 226, 1187–1207, 2018.

Baidya Roy, S., Pacala, S. W., and Walko, R.: Can large wind farms affect local meteorology?, Journal of Geophysical Research: Atmospheres, 109, 2004.

Bastankhah, M. and Porté-Agel, F.: A new analytical model for wind-turbine wakes, Renewable energy, 70, 116–123, 2014.

Bastankhah, M. and Porté-Agel, F.: Experimental and theoretical study of wind turbine wakes in yawed conditions, Journal of Fluid Mechanics, 806, 506–541, 2016.

Bastankhah, M., Welch, B. L., Martínez-Tossas, L. A., King, J., and Fleming, P.: Analytical solution for the cumulative wake of wind turbines in wind farms, Journal of Fluid Mechanics, 911, A53, 2021.

Bastankhah, M., Mohammadi, M. M., Lees, C., Diaz, G. P. N., Buxton, O. R., and Ivanell, S.: A fast-running physics-based wake model for a semi-infinite wind farm, Journal of Fluid Mechanics, 985, A43, 2024.

Bodini, N., Zardi, D., and Lundquist, J. K.: Three-dimensional structure of wind turbine wakes as measured by scanning lidar, Atmospheric Measurement Techniques, 10, 2881–2896, 2017.

Brugger, P., Fuertes, F. C., Vahidzadeh, M., Markfort, C. D., and Porté-Agel, F.: Characterization of wind turbine wakes with Nacelle-Mounted Doppler LiDARs and model validation in the presence of wind veer, Remote Sensing, 11, 2247, 2019.

Carbajo Fuertes, F., Markfort, C. D., and Porté-Agel, F.: Wind turbine wake characterization with nacelle-mounted wind lidars for analytical wake model validation, Remote sensing, 10, 668, 2018.

Chamorro, L., Hill, C., Morton, S., Ellis, C., Arndt, R., and Sotiropoulos, F.: On the interaction between a turbulent open channel flow and an axial-flow turbine, Journal of Fluid Mechanics, 716, 658–670, 2013.

Cheng, W.-C. and Porté-Agel, F.: A Simple Physically-Based Model for Wind-Turbine Wake Growth in a Turbulent Boundary Layer, Boundary-Layer Meteorology, 169, 1–10, 2018.

Cheng, Y., Zhang, M., Zhang, Z., and Xu, J.: A new analytical model for wind turbine wakes based on Monin-Obukhov similarity theory, Applied Energy, 239, 96–106, 2019.

https://doi.org/10.5194/wes-2026-210
Preprint. Discussion started: 17 November 2026
© Author(s) 2026. CC BY 4.0 License.

Cheung, L., Yalla, G., Brown, K., Develder, N., Hsieh, A., Herges, T., Houck, D., Maniaci, D., Sakievich, P., and Abraham, A.: Modification of wind turbine wakes by large-scale, convective atmospheric boundary layer structures, Journal of Renewable and Sustainable Energy, 16, 2024.

Churchfield, M. J. and Sirnivas, S.: On the effects of wind turbine wake skew caused by wind veer, in: 2018 wind energy symposium, p. 0755, 2018.

Churchfield, M. J., Lee, S., Michalakes, J., and Moriarty, P. J.: A numerical study of the effects of atmospheric and wake turbulence on wind turbine dynamics, Journal of turbulence, p. N14, 2012.

Churchfield, M. J., Lee, S., Moriarty, P. J., Hao, Y., Lackner, M. A., Barthelmie, R., Lundquist, J. K., and Oxley, G.: A comparison of the dynamic wake meandering model, large-eddy simulation, and field data at the Egmond aan Zee offshore wind plant, in: 33rd Wind Energy Symposium, p. 0724, 2015.

Crespo, A. and Hernández, J.: Turbulence characteristics in wind-turbine wakes, Journal of wind engineering and industrial aerodynamics, 61, 71–85, 1996.

Dammann, T., Dangi, N., Van Wingerden, J.-W., and Yu, W.: Benchmark Study on Rotor Performance, Wake Dynamics, and Atmospheric Boundary Layers using NREL SOWFA-6 and AMR-WIND, in: Journal of Physics: Conference Series, vol. 3016, p. 012034, IOP Publishing, 2025.

Dar, A. S. and Bachynski-Polić, E. E.: Comparison of analytical models for wind turbine wakes under thermal stability and veer effects, in: Journal of Physics: Conference Series, vol. In Press, IOP Publishing, 2026.

Dar, A. S., Gertler, A. S., and Porté-Agel, F.: An experimental and analytical study of wind turbine wakes under pressure gradient, Physics of Fluids, 35, 2023.

Dar, A. S., Kotsarinis, K., and Porté-Agel, F.: Effect of thermal stability on wind turbine wakes: an experimental and analytical study, Boundary-Layer Meteorology, 192, 27, 2026.

Deardorff, J. W.: Stratocumulus-capped mixed layers derived from a three-dimensional model, Boundary-layer meteorology, 18, 495–527, 1980.

Doosttalab, A., Siguenza-Alvarado, D., Pulletikurthi, V., Jin, Y., Bocanegra Evans, H., Chamorro, L. P., and Castillo, L.: Interaction of low-level jets with wind turbines: On the basic mechanisms for enhanced performance, Journal of Renewable and Sustainable Energy, 12, 2020.

Dörenkämper, M., Witha, B., Steinfeld, G., Heinemann, D., and Kühn, M.: The impact of stable atmospheric boundary layers on wind-turbine wakes within offshore wind farms, Journal of Wind Engineering and Industrial Aerodynamics, 144, 146–153, 2015.

Doubrawa, P., Martinez-Tossas, L. A., Quon, E., Moriarty, P., and Churchfield, M. J.: Comparison of mean and dynamic wake characteristics between research-scale and full-scale wind turbines, in: Journal of Physics: Conference Series, vol. 1037, p. 072053, IOP Publishing, 2018.

Du, B., Ge, M., Zeng, C., Cui, G., and Liu, Y.: Influence of atmospheric stability on wind-turbine wakes with a certain hub-height turbulence intensity, Physics of Fluids, 33, 2021.

Du, B., Ge, M., and Liu, Y.: A physical wind-turbine wake growth model under different stratified atmospheric conditions, Wind Energy, 25, 1812–1836, 2022.

Du, B., Ge, M., Li, X., and Liu, Y.: Evaluation of wake superposition methods for wind-farm flow and power prediction, in: Journal of Physics: Conference Series, vol. 3016, p. 012036, IOP Publishing, 2025.

Ekman, V. W.: On the influence of the earth's rotation on ocean-currents., 1905.

https://doi.org/10.5194/wes-2026-210
Preprint. Discussion started: 17 November 2026
© Author(s) 2026. CC BY 4.0 License.

Englberger, A. and Lundquist, J. K.: How does inflow veer affect the veer of a wind-turbine wake?, in: Journal of Physics: Conference Series, vol. 1452, p. 012068, IOP Publishing, 2020.

Foundation, T. O.: OpenFOAM-6, https://openfoam.org/version/6, 2018.

Frandsen, S., Barthelmie, R., Pryor, S., Rathmann, O., Larsen, S., Højstrup, J., and Thøgersen, M.: Analytical modelling of wind speed deficit in large offshore wind farms, Wind Energy: An International Journal for Progress and Applications in Wind Power Conversion Technology, 9, 39–53, 2006.

Frandsen, S. T.: Turbulence and turbulence-generated structural loading in wind turbine clusters, 2007.

Gadde, S. N. and Stevens, R. J.: Effect of Coriolis force on a wind farm wake, in: Journal of physics: Conference series, vol. 1256, p. 012026, IOP Publishing, 2019.

Gadde, S. N. and Stevens, R. J.: Interaction between low-level jets and wind farms in a stable atmospheric boundary layer, Physical review fluids, 6, 014 603, 2021.

Gaertner, E., Rinker, J., Sethuraman, L., Zahle, F., Anderson, B., Barter, G., Abbas, N., Meng, F., Bortolotti, P., Skrzypinski, W., et al.: Definition of the IEA 15-MW offshore reference wind turbine, 2020.

Gao, X., Li, B., Wang, T., Sun, H., Yang, H., Li, Y., Wang, Y., and Zhao, F.: Investigation and validation of 3D wake model for horizontal-axis wind turbines based on field measurements, Applied Energy, 260, 114 272, 2020.

Ge, M., Wu, Y., Liu, Y., and Li, Q.: A two-dimensional model based on the expansion of physical wake boundary for wind-turbine wakes, Applied energy, 233, 975–984, 2019.

Ghaisas, N. S., Archer, C. L., Xie, S., Wu, S., and Maguire, E.: Evaluation of layout and atmospheric stability effects in wind farms using large-eddy simulation, Wind Energy, 20, 1227–1240, 2017.

Hanna, S.: Applications in air pollution modeling, in: Atmospheric Turbulence and Air Pollution Modelling: A Course Held in the Hague, 21–25 September, 1981, pp. 275–310, Springer, 1984.

Hansen, K. S., Barthelmie, R. J., Jensen, L. E., and Sommer, A.: The impact of turbulence intensity and atmospheric stability on power deficits due to wind turbine wakes at Horns Rev wind farm, Wind Energy, 15, 183–196, 2012.

Hultmark, M., Vallikivi, M., Bailey, S. C. C., and Smits, A.: Turbulent pipe flow at extreme Reynolds numbers, Physical review letters, 108, 094 501, 2012.

Ishihara, T. and Qian, G.-W.: A new Gaussian-based analytical wake model for wind turbines considering ambient turbulence intensities and thrust coefficient effects, Journal of Wind Engineering and Industrial Aerodynamics, 177, 275–292, 2018.

Jensen, N. O.: A note on wind generator interaction, Risø National Laboratory, 1983.

JHU: Windfarm datasets, https://turbulence.idies.jhu.edu/datasets/windfarms, 2026.

Jin, Y., Liu, H., Aggarwal, R., Singh, A., and Chamorro, L. P.: Effects of freestream turbulence in a model wind turbine wake, Energies, 9, 830, 2016.

Johlas, H. M., Martínez-Tossas, L. A., Schmidt, D. P., Lackner, M. A., and Churchfield, M. J.: Large eddy simulations of floating offshore wind turbine wakes with coupled platform motion, in: Journal of Physics: Conference Series, vol. 1256, p. 012018, IOP Publishing, 2019.

Johlas, H. M., Schmidt, D. P., and Lackner, M. A.: Large eddy simulations of curled wakes from tilted wind turbines, Renewable Energy, 188, 349–360, 2022.

Katic, I., Højstrup, J., and Jensen, N. O.: A simple model for cluster efficiency, in: European wind energy association conference and exhibition, vol. 1, pp. 407–410, A. Raguzzi Rome, Italy, 1986.

https://doi.org/10.5194/wes-2026-210
Preprint. Discussion started: 17 November 2026
© Author(s) 2026. CC BY 4.0 License.

Krutova, M., Paskyabi, M. B., Nielsen, F. G., and Reuder, J.: Evaluation of Gaussian wake models under different atmospheric stability conditions: Comparison with large eddy simulation results, in: Journal of Physics: Conference Series, vol. 1669, p. 012016, IOP Publishing, 2020.

Li, L., Huang, Z., Ge, M., and Zhang, Q.: A novel three-dimensional analytical model of the added streamwise turbulence intensity for wind-turbine wakes, Energy, 238, 121 806, 2022.

Li, L., Wang, B., Ge, M., Huang, Z., Li, X., and Liu, Y.: A novel superposition method for streamwise turbulence intensity of wind-turbine wakes, Energy, 276, 127 491, 2023.

Lissaman, P.: Energy effectiveness of arbitrary arrays of wind turbines, Journal of Energy, 3, 323–328, 1979.

Liu, H., Hayat, I., Jin, Y., and Chamorro, L. P.: On the evolution of the integral time scale within wind farms, Energies, 11, 93, 2018.

Liu, X., Li, Z., Yang, X., Xu, D., Kang, S., and Khosronejad, A.: Large-eddy simulation of wakes of waked wind turbines, Energies, 15, 2899, 2022.

Machefaux, E., Larsen, G. C., Koblitz, T., Troldborg, N., Kelly, M. C., Chougule, A., Hansen, K. S., and Rodrigo, J. S.: An experimental and numerical study of the atmospheric stability impact on wind turbine wakes, Wind Energy, 19, 1785–1805, 2016.

Martinez-Tossas, L. A., Churchfield, M. J., Yilmaz, A. E., Sarlak, H., Johnson, P. L., Sørensen, J. N., Meyers, J., and Meneveau, C.: Comparison of four large-eddy simulation research codes and effects of model coefficient and inflow turbulence in actuator-line-based wind turbine modeling, Journal of Renewable and Sustainable Energy, 10, 2018.

Meneveau, C.: Big wind power: seven questions for turbulence research, Journal of Turbulence, 20, 2–20, 2019.

Meneveau, C. and Marusic, I.: Generalized logarithmic law for high-order moments in turbulent boundary layers, Journal of Fluid Mechanics, 719, R1, 2013.

Mishra, A., Arya, N., and Bhattacharya, A.: Wake steering of wind turbine in the presence of a two-dimensional hill, Physics of Fluids, 36, 2024.

Moeng, C.-H.: A large-eddy-simulation model for the study of planetary boundary-layer turbulence, Journal of Atmospheric Sciences, 41, 2052–2062, 1984.

Monin, A. S. and Obukhov, A. M.: Basic laws of turbulent mixing in the surface layer of the atmosphere, Contrib. Geophys. Inst. Acad. Sci. USSR, 151, e187, 1954.

Narasimhan, G., Gayme, D. F., and Meneveau, C.: Analytical wake modeling in atmospheric boundary layers: Accounting for wind veer and thermal stratification, in: Journal of Physics: Conference Series, vol. 2767, p. 092018, IOP Publishing, 2024.

Niayifar, A. and Porté-Agel, F.: Analytical modeling of wind farms: A new approach for power prediction, Energies, 9, 741, 2016.

Ning, X. and Wan, D.: LES study of wake meandering in different atmospheric stabilities and its effects on wind turbine aerodynamics, Sustainability, 11, 6939, 2019.

Ning, X., Krutova, M., and Bakhoday-Paskyabi, M.: Analysis of offshore wind spectra and coherence under neutral stability condition using the two LES models PALM and SOWFA, in: Journal of Physics: Conference Series, vol. 2018, p. 012027, IOP Publishing, 2021.

Nouri, R., Vasel-Be-Hagh, A., and Archer, C. L.: The Coriolis force and the direction of rotation of the blades significantly affect the wake of wind turbines, Applied Energy, 277, 115 511, 2020.

NREL: SOWFA-6, https://github.com/NREL/SOWFA-6, 2025a.

NREL: OpenFAST v3.5.0, https://github.com/OpenFAST/openfast, 2025b.

Placidi, M., Hancock, P. E., and Hayden, P.: Wind turbine wakes: experimental investigation of two-point correlations and the effect of stable thermal stability, Journal of Fluid Mechanics, 970, A30, 2023.

https://doi.org/10.5194/wes-2026-210
Preprint. Discussion started: 17 November 2026
© Author(s) 2026. CC BY 4.0 License.

Porté-Agel, F., Bastankhah, M., and Shamsoddin, S.: Wind-turbine and wind-farm flows: a review, Boundary-layer meteorology, 174, 1–59, 2020.

Revaz, T. and Porté-Agel, F.: Large-eddy simulation of wind turbine flows: A new evaluation of actuator disk models, Energies, 14, 3745, 2021.

Schumann, U.: Subgrid scale model for finite difference simulations of turbulent flows in plane channels and annuli, Journal of computational physics, 18, 376–404, 1975.

Scott, R., Martínez-Tossas, L., Bossuyt, J., Hamilton, N., and Cal, R. B.: Evolution of eddy viscosity in the wake of a wind turbine, Wind Energy Science, 8, 449–463, 2023.

Shamsoddin, S. and Porté-Agel, F.: A model for the effect of pressure gradient on turbulent axisymmetric wakes, Journal of Fluid Mechanics, 837, R3, 2018.

Siedersleben, S. K., Lundquist, J. K., Platis, A., Bange, J., Bärfuss, K., Lampert, A., Cañadillas, B., Neumann, T., and Emeis, S.: Micrometeorological impacts of offshore wind farms as seen in observations and simulations, Environmental Research Letters, 13, 124 012, 2018.

Souaiby, M. and Porté-Agel, F.: An improved analytical framework for flow prediction inside and downstream of wind farms, Renewable Energy, 225, 120 251, 2024.

Souaiby, M. and Porté-Agel, F.: Physics-based and stability-aware analytical modeling of wind turbine wakes, Applied Energy, 410, 127 586, 2026.

Stevens, R. J. and Meneveau, C.: Flow structure and turbulence in wind farms, Annual review of fluid mechanics, 49, 311–339, 2017.

Thomsen, K. and Sørensen, P.: Fatigue loads for wind turbines operating in wakes, Journal of wind engineering and industrial aerodynamics, 80, 121–136, 1999.

Tian, L., Song, Y., Xiao, P., Zhao, N., Shen, W., and Zhu, C.: A new three-dimensional analytical model for wind turbine wake turbulence intensity predictions, Renewable Energy, 189, 762–776, 2022.

Trabucchi, D., Trujillo, J.-J., and Kühn, M.: Nacelle-based lidar measurements for the calibration of a wake model at different offshore operating conditions, Energy Procedia, 137, 77–88, 2017.

Vahidi, D. and Porté-Agel, F.: A physics-based model for wind turbine wake expansion in the atmospheric boundary layer, Journal of Fluid Mechanics, 943, A49, 2022.

Veers, P., Dykes, K., Lantz, E., Barth, S., Bottasso, C. L., Carlson, O., Clifton, A., Green, J., Green, P., Holttinen, H., et al.: Grand challenges in the science of wind energy, Science, 366, eaau2027, 2019.

Voutsinas, S., Rados, K., and Zervos, A.: On the analysis of wake effects in wind parks, Wind Engineering, pp. 204–219, 1990.

Wu, S., Archer, C. L., and Mirocha, J. D.: New insights on wind turbine wakes from large-eddy simulation: Wake contraction, dual nature, and temperature effects, Wind Energy, 27, 1130–1151, 2024.

Xiao, P., Tian, L., Zhao, N., Song, Y., Wang, Z., and Lu, X.: An integrated model for predicting wind turbine wake velocity and turbulence intensity under different atmospheric stability regimes, Renewable Energy, 256, 123 904, 2026.

Xiao, S., Zhu, X., Narasimhan, G., Gayme, D. F., and Meneveau, C.: Wind farm dynamics over a diurnal cycle: Analysis of a comprehensive large-eddy simulation, web-services accessible dataset, Journal of Renewable and Sustainable Energy, 17, 2025.

Xie, S. and Archer, C. L.: A numerical study of wind-turbine wakes for three atmospheric stability conditions, Boundary-Layer Meteorology, 165, 87–112, 2017.

Zehtabiyan-Rezaie, N., Justsen, J. P., and Abkar, M.: Wind-farm power prediction using a turbulence-optimized Gaussian wake model, Wind Energy and Engineering Research, 2, 100 007, 2024.

https://doi.org/10.5194/wes-2026-210
Preprint. Discussion started: 17 November 2026
© Author(s) 2026. CC BY 4.0 License.



Zhu, X., Xiao, S., Narasimhan, G., Martinez-Tossas, L. A., Schnaubelt, M., Lemson, G., Yao, H., Szalay, A. S., Gayme, D., and Meneveau, C.: JHTDB-wind: a web-accessible large-eddy simulation database of a wind farm with virtual sensor querying, Wind Energy Science, 10, 2821–2840, 2025.

Zong, H. and Porté-Agel, F.: A momentum-conserving wake superposition method for wind farm power prediction, Journal of Fluid Mechanics, 889, A8, 2020.